AFRL-AFOSR-UK-TR-2020-0027

Characterization of Lean, Turbulent Flames at Gas Turbine Operating Conditions Using Highspeed Laser-Diagnostic Techniques

Isaac Boxx
DEUTSCHES ZENTRUM FUR LUFT- UND RAUMFAHRT E.V.
LINDER HOHE, KA
KOLN, 51147
DE

05/18/2020
Final Report

Air Force Research Laboratory
Air Force Office of Scientific Research
European Office of Aerospace Research and Development
Unit 4515 Box 14, APO AE 09421

REPORT DOCUMENTATION PAGE

Form Approved
OMB No. 0704-0188

1. REPORT DATE *(DD-MM-YYYY)*	2. REPORT TYPE	3. DATES COVERED *(From - To)*
18-05-2020	Final	01 Dec 2015 to 30 Nov 2019

4. TITLE AND SUBTITLE
Characterization of Lean, Turbulent Flames at Gas Turbine Operating Conditions Using Highspeed Laser-Diagnostic Techniques

5a. CONTRACT NUMBER

5b. GRANT NUMBER
FA9550-16-1-0044

5c. PROGRAM ELEMENT NUMBER
61102F

6. AUTHOR(S)
Isaac Boxx

5d. PROJECT NUMBER

5e. TASK NUMBER

5f. WORK UNIT NUMBER

7. PERFORMING ORGANIZATION NAME(S) AND ADDRESS(ES)
DEUTSCHES ZENTRUM FUR LUFT- UND RAUMFAHRT E.V.
LINDER HOHE, KA
KOLN, 51147 DE

8. PERFORMING ORGANIZATION REPORT NUMBER

9. SPONSORING/MONITORING AGENCY NAME(S) AND ADDRESS(ES)
EOARD
Unit 4515
APO AE 09421-4515

10. SPONSOR/MONITOR'S ACRONYM(S)
AFRL/AFOSR IOE

11. SPONSOR/MONITOR'S REPORT NUMBER(S)
AFRL-AFOSR-UK-TR-2020-0027

12. DISTRIBUTION/AVAILABILITY STATEMENT
A DISTRIBUTION UNLIMITED: PB Public Release

13. SUPPLEMENTARY NOTES

14. ABSTRACT
High bandwidth laser imaging demonstrated in turbulent swirl- and bluff-body stabilized flames at pressures of up to 20 bars. Detailed, multi-diagnostic measurements were acquired in swirl- and bluff-body stabilized flames at elevated pressures. These measurements generated significant new insight into the turbulent mixing and flame dynamics, combustion instabilities and flow-flame interaction.
Three external measurement campaigns were completed at universities in the United States. During these campaigns, the research teams of young faculty (sponsored through the AFOSR-BCR program) received both hands-on training and valuable practical experience in the design, setup and operation of sophisticated laser diagnostic systems for combustion research.
Research performed during this project has (at the time of writing) resulted in five peer-reviewed journal papers, with two more currently under review. Several more still in preparation. In addition, it has generated nine conference proceedings.
Finally, the project also provided a unique, hands-on research experience in high bandwidth laser imaging for AFRL scientists Dr. Campbell Carter and Dr. Carrie Noren, who engaged in on-site research collaborations linked to the project.

15. SUBJECT TERMS
eoard, high speed laser disgnostics, cumbustion diagnostics

16. SECURITY CLASSIFICATION OF:			17. LIMITATION OF ABSTRACT	18. NUMBER OF PAGES	19a. NAME OF RESPONSIBLE PERSON
a. REPORT	b. ABSTRACT	c. THIS PAGE			SMITH, DOUGLAS
Unclassified	Unclassified	Unclassified	SAR		19b. TELEPHONE NUMBER *(Include area code)* 314-235-6013

Standard Form 298 (Rev. 8/98)
Prescribed by ANSI Std. Z39.18

Final Performance Report –February 29th, 2020

Award Number: FA9550-16-1-0044

Period of Performance: 1 December, 2015 – 30 November, 2019

Research Title: "Characterization of Lean, Turbulent Flames at Gas Turbine Operating Conditions Using Highspeed Laser-Diagnostic Techniques"

Principal Investigator - Dr. Isaac Boxx

Table of Contents

Summary	4
Introduction	4
Section 1 – Experimental Studies Completed at DLR	5
Section 2 – Multilateral Collaborations with American Universities	32
Conclusions	45
References	46
Publications	47

List of Figures

Figure 1.1.1 – The DLR High-pressure, premixed bluff-body stabilized burner.

Figure 1.1.2 – Bluff-body instrumentation points, with thermocouple locations shown in red.

Figure 1.1.3 – Bluff-body model, including flow straightening channels

Figure 1.1.4 – Physical hardware of the DLR premixed, bluff-body stabilized burner

Figure 1.1.5 - Optical layout for combined PIV and OH-PLIF within the HIPOT Test Facility

Figure 1.1.6 – Sample sequence of OH-PLIF images acquired at flame condition "1i" (P = 3 bars, U_r = 20.6m/s, T_r = 423K, Phi = 0.67).

Figure 1.1.7 – Sample sequence of OH* chemilumienscence images acquired at flame condition "1i" (P = 3 bars, U _r = 20.6m/s, T_r = 423K, Phi = 0.67).

Figure 1.1.8. OH-PLIF (*upper*), velocity field magnitude (*middle*) and axial velocity (lower) fields acquired at flame condition "1i" (P = 3 bars, U_r = 20.6m/s, T_r = 423K, Phi = 0.67).

Figure 1.1.9. Phase-averaged FSD image sequence under strong acoustic forcing, measured in a bluff body burner of similar design, U_r = 9.9m/s, *f* = 160Hz, phi = 0.51. ***Reproduced from Balachandran, et al. (2005)***

Figure 1.1.10 – Ensemble average of OH* chemiluminescence (upper), OH-PLIF signal (middle) and axial velocity (lower) measured at Flame Condition "1i" (P = 3 bars, U _r = 20.6m/s, T_r = 423K, Phi = 0.67).

Figure 1.1.11. - Phase-averaged PIV and OH* measurements of flames measured at Condition 1c (upper) and 1F (lower). This corresponds to P = 3 bars, U = 10.1m/s and ϕ = 0.77 and 1.0, respectively.

Figure 1.1.12 – Average OH-PLIF (upper) and OH*-Chemiluminescence (lower) measured in flames at Conditions 2b, 2c, 2h and 2m, which correspond to 5, 10, 15, and 20 bars. Flow is from left to right.

Figure 1.1.13 - OH*-Chemiluminescence image sequences measured in flames at Conditions 2b, 2c, 2h and 2m, which correspond to 5, 10, 15, and 20 bars. Flow is from left to right. Time between frames is 2ms.

Figure 1.1.14 - OH-PLIF image sequences measured in flames at Conditions 2b, 2c, 2h and 2m, which correspond to 5, 10, 15, and 20 bars. Flow is from left to right. Time between frames is 2ms.

Figure 1.1.15 – Signal-to-Noise ratio of mean OH-PLIF images vs chamber pressure.

Figure 1.2.1 –Apparatus used in Measurement Series A

Figure 1.2.2 – Dual-swirl gas turbine model combustor

Figure 1.2.3 – Mean flow fields for the nonreacting (upper) and reacting (lower) flow conditions at each air staging.

Figure 1.2.4 – Peak frequency measured at a monitor point on the axial centerline of the burner, 5mm downstream of the nozzle. Black dots represent the nonreacting flow, and red the reacting.

Figure 1.2.5 – The dominant eigenmodes measured in the reacting flow condition with 50/50 air split.

Figure 1.2.6 – Time-series measurements of a) Acoustic pressure, b) OH* Chemiluminescence and c) r.m.s. axial velocity fluctuations in the combustor.

Figure 1.2.7 Mean OH* chemiluminescence (upper) and axial velocity (lower) fields. The left and right columns correspond to the flame in the stable- and the excited state, respectively.

Figure 1.2.8. Morlet-amplitude (envelope) scalogram for axial velocity in the flame region.

Figure 1.2.9 – Mean (upper) and fluctuating (lower) acetone-PLIF measurements for the non-reacting (left) and reacting (right) flow condition.

Figure 1.2.10 – POD analysis of non-reacting acetone-PLIF distributions: energy distribution of the POD modes and power spectra of temporal POD coefficients.

Figure 1.2.11 – Acetone-PLIF distributions for isothermal conditions, phase averaged with respect to the 384 Hz frequency of the dominant flow structure, a precessing vortex core.

Figure 1.2.12 – POD analysis of reacting flow acetone-PLIF distributions: energy distribution of the POD modes and power spectra of temporal POD coefficients based on the acetone-PLIF data.

Figure 1.2.13 – Acetone-PLIF distributions for the reacting flow test condition, phase averaged with respect to the a) 874 Hz frequency of the symmetric, toroidal vortex shedding and b) 453 Hz frequency of the PVC structures.

Figure 1.2.14 - Sample OH-PLIF images from the dual swirl burner in the HIPOT. Rows 1-4 show 5 consecutive images (delta-t = 0.1 ms) at pressures of 5, 10, 13, and15 bars.

Figure 1.2.15 – Photographs showing the experimental hardware.

Figure 2.1.1 – Penn State Dual Flame Burner.

Figure 2.1.2 – High bandwidth laser imaging experiment configuration.

Figure 2.1.3 – High bandwidth laser imaging experiment at Professor O'Connor's laboratory at the Pennsylvania State University.

Figure 2.2.1 – a) UCF High speed blow-down wind-tunnel facility, b) Bluff-body stabilized burner

Figure 2.2.2 – Optical Diagnostics System. Left – Imaging Systems, Right – Laser illumination system.

Figure 2.2.3 – High bandwidth laser imaging experiment at Professor Ahmed's laboratory at the University of Central Florida.

Figure 2.2.4 – Instantaneous vorticity contour, flame boundary, and the overlay of strain rate on the flame boundary. Time t* = 0 represents stable flame and t* = 1 is complete blow-out.

Figure 2.3.1 – Schematic of the Jet in Vitiated Coflow (JIVCF) Burner studied at NC-State University.

Figure 2.3.2 – Stereo-PIV / HCHO-PLIF experiment implemented at Professor Narayanaswamy's laboratory at NC State University.

Figure 2.3.3 – PIV / PSP experiment implemented at Professor Narayanaswamy's laboratory at NC State University. In this configuration, the upper camera is used for near-wall PIV imaging and the lower camera images the pressure sensitive paint.

Figure 2.3.4 – Overlay of the velocity and pressure field with a shock wave incident on a plate at Mach 2.5

Summary

In December, 2015 a collaborative research effort between the German Aerospace Center (DLR) and the Air Force Research Laboratory (AFRL) was initiated. This project had the following three key goals;

1. To explore the viability of applying simultaneous, kHz-rate stereoscopic particle image velocimetry (stereo-PIV) and planar laser-induced fluorescence of hydroxyl (OH-PLIF) in a lean, turbulent swirl-stabilized flame at pressures ranging from 5 bars up to those found in a modern gas turbine combustor.
2. To apply these diagnostics to study flow-flame interactions leading to combustion instability and thermo-acoustic pulsation in the DLR Dual-Swirl Burner and a premixed, bluff-body stabilized flame at elevated pressure conditions.
3. To share the knowledge and experience gained in this project with members of the AFOSR-Basic Combustion Research Program and the wider combustion research community through a series of one-on-one, on-site technical collaborations.

This project concluded on the 30th of November, 2019. All key objectives were achieved.

High bandwidth laser imaging demonstrated in turbulent swirl- and bluff-body stabilized flames at pressures of up to 20 bars. Detailed, multi-diagnostic measurements were acquired in swirl- and bluff-body stabilized flames at elevated pressures. These measurements generated significant new insight into the turbulent mixing and flame dynamics, combustion instabilities and flow-flame interaction.

Three external measurement campaigns were completed at universities in the United States. During these campaigns, the research teams of young faculty (sponsored through the AFOSR-BCR program) received both hands-on training and valuable practical experience in the design, setup and operation of sophisticated laser diagnostic systems for combustion research.

Research performed during this project has (at the time of writing) resulted in five peer-reviewed journal papers, with two more currently under review. Several more still in preparation. In addition, it has generated nine conference proceedings.

Finally, the project also provided a unique, hands-on research experience in high bandwidth laser imaging for AFRL scientists Dr. Campbell Carter and Dr. Carrie Noren, who engaged in on-site research collaborations linked to the project.

Introduction

During this project, a total of five on-site measurement campaigns were performed on three burner configurations in two different test facilities. In addition, three off-site measurement campaigns were performed in collaboration AFOSR-sponsored research groups at universities in the United States. Given the diversity of research efforts undertaken in the project, this Final Performance Report is organized in two thematic sections. The first section will detail research efforts undertaken at the DLR Institute of Combustion Technology in Stuttgart. This will be split into two subsections, each devoted to a specific burner geometry. The second section of the report will detail research efforts undertaken in collaboration with teams in the United States. This section will contain three subsections, with each devoted to a specific collaborative research effort. Finally, a short summary/conclusion is provided.

Section 1.1 – High bandwidth laser imaging measurements of premixed, turbulent bluff-body stabilized flames at elevated pressure conditions

Introduction / Background

The work plan for Phase 1 of this project called for the design and construction of a premixed, bluff-body stabilized burner with a cylindrical centerbody and annular reactant flow. The burner would be used to generate premixed turbulent flames with highly reproducible turbulence characteristics and boundary conditions. The flames generated with this burner were to be used both to study turbulent flame dynamics and to characterize the performance of highspeed imaging diagnostics at elevated temperature and pressure conditions.

Burner Design

The DLR high-pressure, premixed, axisymmetric bluff-body stabilized burner is shown in Figure 1.1.1. It consists of five main components; 1) a fuel-air mixing channel (turquoise), 2) a tubular flow channel (blue), 3) a cylindrical bluff body, equipped with active cooling and a conically-flared tip (to accelerate the reactants and thereby prevent flashback) (turquoise), 4) an actively cooled adaptor mount (grey) and 5) an optically accessible combustion chamber (not shown). These components are mounted within the pressure vessel of the DLR-HIPOT test-rig, to enable operation at elevated pressure and with reactant pre-heat.

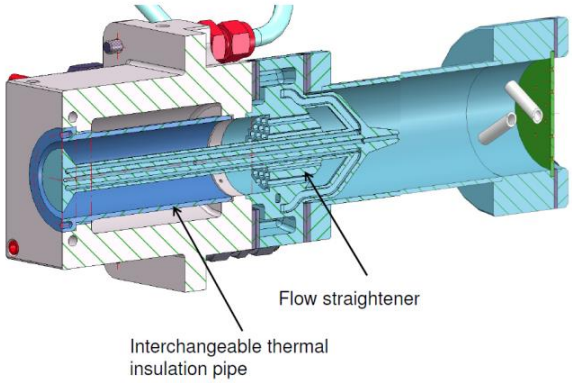

Figure 1.1.1 – The DLR High-pressure, premixed bluff-body stabilized burner.

The central bluff-body is designed with internal channels to enable the passage of gaseous or liquid coolant. This coolant was considered essential to ensuring the burner would survive the intense thermal loads generated by the burner at high pressure conditions. In addition, the coolant would enable us to maintain a constant bluff-body surface temperature and thereby control (and systematically vary) heat-transfer from recirculation zone into the bluff body. This unique capability was designed to yield a well-defined test case the development and validation of conjugate heat transfer models for gas turbine combustors.

Figure 1.1.2 shows a cutaway sketch of the cylindrical bluff-body. Visible in this figure are both the coolant channels and the locations of two thermocouple probes. The first of these is mounted in a channel aligned with the axis of the bluff-body and is used to monitor temperature just below the tip of the bluff-body. The second thermocouple is mounted in a channel along the outer surface of the bluff-body and is used to monitor the temperature at the base of the conical tip. This pair of thermocouples is designed to ensure the safe operation of the burner, i.e. to avoid operational

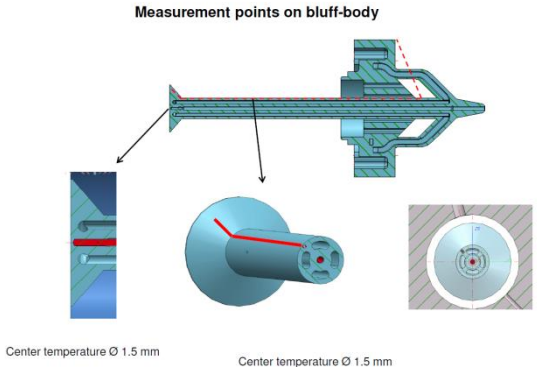

Figure 1.1.2 – Bluff-body instrumentation points, with thermocouple locations shown in red.

points that threaten to melt the bluff-body and to detect flame propagation into the cylindrical flow channel (i.e. flashback). They also provide a basis for the estimation of heat transfer from the recirculation zone of the flame into the bluff-body.

Figure 1.1.3 illustrates the flow conditioning used to ensure straight and axisymmetric flow into the burner. At the base of the bluff body, reactants enter the flow channel via a set of flow straightening channels. These channels are hexagonal in cross-section and have streamlined entrance sections. To minimize flow asymmetry, the (four) coolant channels and central thermocouple probe channel are designed to be both streamlined and axisymmetric. The actual burner hardware is shown in Figure 1.1.4.

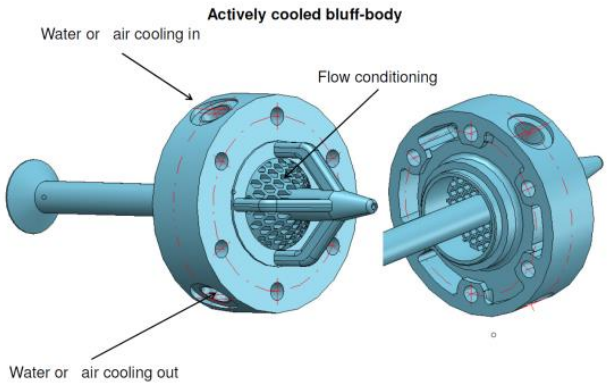

Figure 1.1.3 – Bluff-body model, including flow straightening channels

Figure 1.1.4 – Physical hardware of the DLR premixed, bluff-body stabilized burner

High-Bandwidth Laser Imaging System

The measurement apparatus used in this study is sketched in Figure 1.1.5. It consists of a kHz acquisition-rate stereoscopic PIV system, a kHz acquisition-rate OH-PLIF system, a kHz acquisition-rate OH* chemiluminescence imaging system, and a fast-response piezoresistive pressure transducer. These systems are described (separately) below.

Stereo-PIV System

The stereoscopic-PIV system consists of a dual-cavity, diode-pumped, solid-state, frequency-doubled Nd:YAG laser (Edgewave, IS200-2-LD), producing pulses of up to 9 mJ (each) at 10 kHz, and a pair of CMOS cameras (Phantom V1212, with 1280 by 800 pixels) with 72 GB of onboard memory, sufficient for about 4 seconds of recording time at full resolution and 10-kHz acquisition rate. The PIV cameras were equipped with 200-mm focal-length, f/4 macro objective lenses (Nikon AF-Micro Nikkor) and a 532-nm-bandpass interference filter to suppress background flame luminosity. In the present study, the cameras were operated in dual-frame mode at a reduced image size (640 × 800 pixels), which gave a field of view of 48 × 60 mm.

Three cylindrical lenses are used to form the PIV laser sheet of approximately 30 mm (high) × 1 mm (thick) at the probe region. The PIV cameras were mounted on Scheimpflug adapters to mitigate the image blur associated with off-axis imaging. Inert TiO_2 particles (~1 μm in size) were used as a flow tracer.

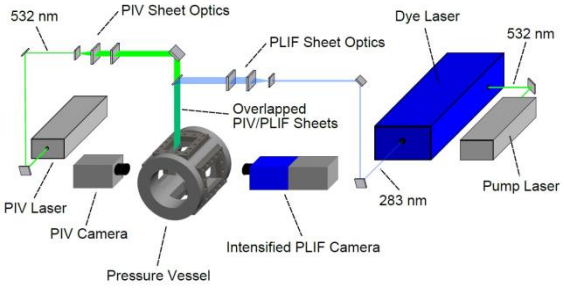

Figure 1.1.5 - Optical layout for combined PIV and OH-PLIF within the HIPOT Test Facility.

Velocity vectors were determined via cross-correlation of image pairs. This was accomplished using a commercially available software package (LaVision Davis 8.4) with a multi-pass adaptive window offset cross-correlation function. The final interrogation window size and overlap were 24 × 24 pixels and 50% respectively for a spatial resolution of 1.5 mm/vector and vector spacing of 0.75 mm.

OH-PLIF System

The OH-PLIF system consists of a *i*) frequency-doubled, Q-switched, diode-pumped solid state Nd:YAG laser (Edgewave IS400-2-L, delivering up to 135 W at 532 nm), *ii*) a frequency-doubled dye laser (pumped by the YAG laser), and *iii*) an intensified CMOS camera system. The dye laser system (Sirah Credo, upgraded with funds supplied through this project) can produce up to 7 W (on average, giving 0.7 mJ/pulse), at the frequency-doubled wavelength of 283 nm and a pulse-repetition frequency of 10 kHz. During one of the two measurement campaigns completed with this burner though, the output was limited to approximately 1.3 W at 283 nm. This was the result of a laser malfunction that resulted in the warping of a mirror holder in the dye laser. To avoid permanent damage to the laser before this fault could be repaired, it was necessary to operate it at reduced power during these measurements.

The dye laser was tuned to excite the $Q_1(9)$ and $Q_2(8)$ lines of the $A^2\Sigma^+ – X^2\Pi$ ($v'=1,v''=0$) band. These transitions merge at high pressure due to increased collisional line broadening, which mitigates to some degree fluorescence signal loss due to collisional line broadening. The laser wavelength was monitored continuously using a setup consisting of *i*) a laminar reference flame, *ii*) a photomultiplier tube coupled to a 0.1-m monochromator for fluorescence detection, and *iii*) a digital oscilloscope; in this way we maintained accurate wavelength tuning (which is critical for good PLIF signal strength). The LeCroy-Teledyne oscilloscope (which is a PC running an oscilloscope application) was configured with a device to transmit its signals to the control room to provide remote operation; this too was critical in robust operation of the PLIF system during operation of the HIPOT.

The 283-nm PLIF excitation beam is formed into a sheet approximately 40 mm (high) × 0.2 mm (thick) using three fused-silica, cylindrical lenses (all *anti-reflective* coated to maximize transmission), and the OH-PLIF and PIV laser sheets are overlapped by passing the PIV sheet through the final OH-PLIF turning mirror.

Fluorescence from the A–X (0,0) band was acquired with a CMOS camera (LaVision HSS8), an external two-stage intensifier (LaVision HS-IRO), and a Halle 64-mm focal length, f/2 UV lens. Elastic scattering (at 283 nm from the PIV seed particles) was blocked with the use of a high-transmission (> 80% at 310 nm) bandpass filter while background flame emission is further attenuated with a 100-ns intensifier gate.

OH Chemiluminescence Imaging System*

A second intensified camera—placed opposite to the PLIF camera (i.e. on the other side of the high-pressure chamber) was employed to record OH* chemiluminescence (radiation from excited-state species formed through chemical reaction, the same process that produces the blue color of a Bunsen flame); OH* chemiluminescence has been shown to be an approximate marker for combustion heat release, but the measurement is *line-of-sight* integrated. The camera for chemiluminescence detection was a high-speed CMOS imaging system (LaVision HSS8) equipped with an external, two-stage, lens-coupled intensifier (LaVision HS-IRO) and fitted with a 45 mm focal length, f/1.8 objective (Cerco) and a high-transmission, band-pass interference filter. The integration time for the chemiluminescence signal (equaling the intensifier gate time) was 25 μs.

Flames Studied

Two series of experiments were completed with this burner. One series was designed to characterize the effect of various operating parameters on the structure and dynamics of flames generated in the bluff-body stabilized burner. The second series was designed to test and characterize the performance of the laser imaging system in turbulent flames at increasing chamber pressure.

These measurements were completed in collaboration with AFRL/RDLT Research Engineer Dr. Carrie Noren. Dr. Noren was hosted at the DLR Institute for Combustion Technology for a period of 24 months through the US Air Force "Engineers and Scientists Exchange Program" (ESEP). At no additional cost to the project, Dr. Noren's participation in this study was valuable to both the project itself and to the US Air Force, inasmuch as she gained valuable training and first-hand experience in the design, setup and operation of high bandwidth laser imaging diagnostics and a high pressure combustion test rig.

Table 1 outlines the operating conditions tested in the first measurement series. The test matrix was designed to characterize the effect of equivalence ratio, reactant inflow velocity and preheat temperature on the structure and dynamics of flames generated in this burner. Pressure was held constant at 3 bars (absolute) for this series of measurements. Equivalence ratio was varied from $\phi = 0.67$ (lean) to $\phi = 1.25$ (rich). Flames operated without preheat (i.e. with reactant temperature at ca. 300 K) were run with reactant inflow velocity of 10.1m/s. Flames with reactant preheat (T = 150 C or 423 K) were run with reactant inflow velocities of 20.6 m/s.

Table 1 – Flame Conditions Measured in Series 1				
Without Reactant Preheat (T = 293K)				
Condition	Pressure (bars)	Equivalence Ratio - ϕ	Bulk Velocity (m/s)	Thermal Load (kW)
1a	3	0.67	10.1	30.3
1b	3	0.71	10.1	31.7
1c	3	0.77	10.1	34.5
1d	3	0.83	10.1	37.1
1e	3	0.91	10.1	40.4
1f	3	1.00	10.1	44.7
1g	3	1.11	10.1	48.5
1h	3	1.25	10.1	54.1
With Reactant Preheat (T = 423K)				
1i	3	0.67	20.6	44.6
1j	3	0.71	20.6	47.8
1k	3	0.77	20.6	51.5
1l	3	0.83	20.6	55.8

Table 2 outlines the operating conditions tested in the second measurement series. The test matrix was designed to characterize the effect of increasing chamber pressure on signal and noise levels measured using the high bandwidth laser imaging system. Flames were measured at chamber pressures ranging from 1 bar (atmospheric pressure) to 20 bars. Reactant inflow velocity was held constant at 10 m/s for all cases. For pressures up to 15 bars, equivalence ratio was held constant at $\phi = 0.83$. For pressures between sixteen and 20 bars, equivalence ratio was held constant at $\phi = 0.77$. Although this change in equivalence ratio may be expected to influence the flame temperature (and therefore the OH concentration), the change was necessary in order for the flame to reach 20 bars pressure, while remaining within the safe operational limits of the HIPOT test rig.

Table 2 – Flame Conditions Measured in Series 2				
Without Reactant Preheat				
Condition	Pressure (bars)	Equivalence Ratio - ϕ	Bulk Velocity (m/s)	Thermal Load (kW)
2a	1	0.83	10	14.8
2b	5	0.83	10	66.3
2c	10	0.83	10	132.7
2d	11	0.83	10	146.2
2e	12	0.83	10	159.6
2f	13	0.83	10	172.8
2g	14	0.83	10	186.2
2h	15	0.83	10	198.6
2i	16	0.77	10	196.4
2j	17	0.77	10	208.5
2k	18	0.77	10	220.9
2l	19	0.77	10	233.7
2m	20	0.77	10	245.2

Measurement Series 1

The DLR premixed, bluff-body burner was designed to generate highly reproducible, premixed turbulent flames with well-defined boundary conditions at elevated pressure conditions. In this regard, the burner achieved its primary objective. The burner did generate such flames. Unfortunately, at all flow conditions at which we operated the burner these flames showed strong, self-excited thermoacoustic oscillation. This manifested as a strong axial pulsation or "puffing" of the flame, wherein the flames would roll up as vortex rings shed from the lip of the bluff-body and burn out downstream. Although this is not what the burner was originally designed to produce, the flames nonetheless constitute an interesting test case for the study of flames at conditions of limit-cycle thermoacoustic oscillation under elevated pressure conditions. In addition, the reproducibility of the measurements makes them a good test case for characterizing the performance of the high bandwidth laser imaging system developed in this project.

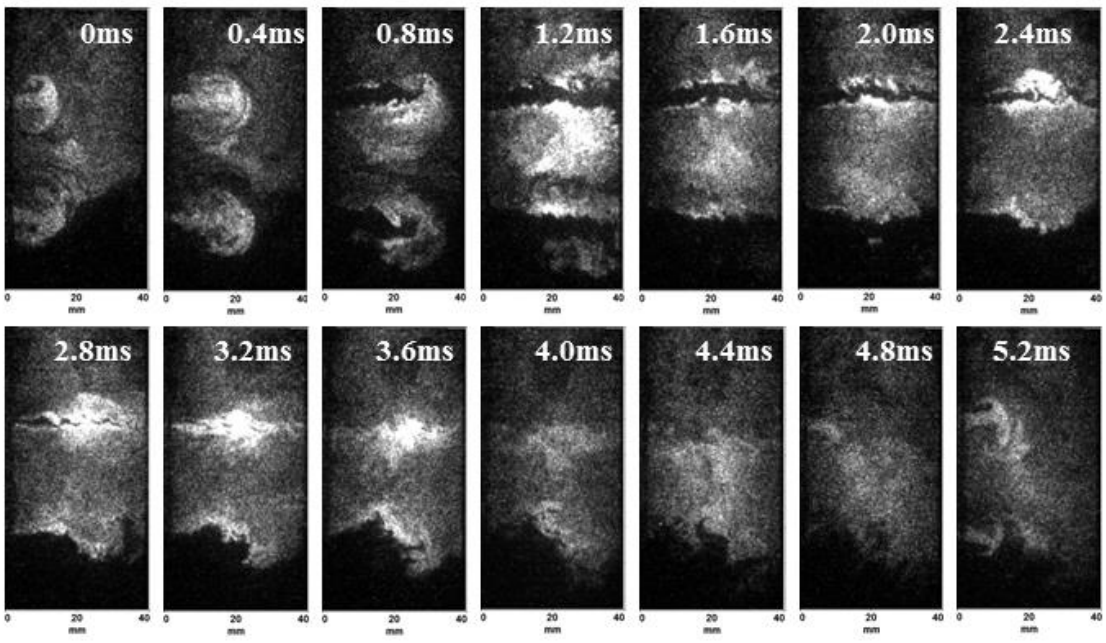

Figure 1.1.6 – Sample sequence of OH-PLIF images acquired at flame condition "1i" (P = 3 bars, U_r = 20.6m/s, T_r = 423K, Phi = 0.67).

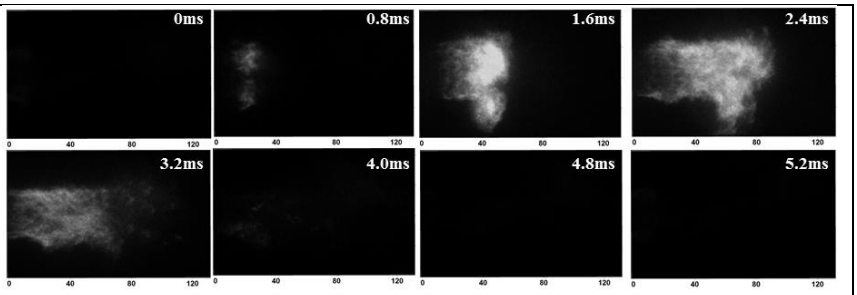

Figure 1.1.7 – Sample sequence of OH* chemilumienscence images acquired at flame condition "1i" (P = 3 bars, U _r = 20.6m/s, T_r = 423K, Phi = 0.67). Images correspond to those in Figure 1.1.3

Figures 1.1.6 and 1.1.7 show a representative sequence of OH-PLIF and OH* chemiluminescence images (respectively) acquired in a flame at condition "1i". As noted in Table 1, this corresponds to bulk flow velocity of 20.6m/s, equivalence ratio of 0.67 and reactant preheat to 423K at a combustor pressure of 3bars. In Figure 1.1.6, every forth measurement of the sequence in displayed. In Figure 1.1.7, it is every eighth frame. Both image sequences show the same measurement period, to enable a direct comparison of the OH* and OH-PLIF measurements. The duration of the image sequence was chosen so as to display approximately one full cycle of the dominant (192Hz) thermoacoustic oscillation.

In the first frame of Figure 1.1.6 (t = 0ms), we observe a pair of mushroom-shaped structures in the OH-PLIF images, equidistant from the axial centerline of the image. Note that the structures appear uniformly filled with OH-signal. At ground-state OH is only found at moderate-to-high temperatures (T > ≈1500K), this structure clearly indicates the presence of burned gas in the reactant stream at the dump plane for this point in the cycle. In the second frame (t = 0.4ms), we observe that this structure has moved downstream and distorted somewhat from its initial, round shape into a more elongated shape. OH-LIF signal is still observable throughout the structure. By 0.8ms, the mushroom shaped structures are no longer apparent, and the OH-LIF signal is no longer observable in the reactant stream. Between 0.8 and 2ms, the lower temperature (as indicated by a lack of OH-LIF signal) reactant stream is visible on either side of the centerline and then, beginning at 2.4ms, it begins to pinch off and propagate out of the field of view by t = 3.2ms. For the next 2ms, a relatively uniform OH-LIF signal is observable across the entire field of view, indicating the presence of hot, burned gases but no active reaction zones (identifiable through superequilibrium OH-concentrations and a sharp signal gradient).

Comparing the OH* measurements in Figure 1.1.7 with the corresponding OH-PLIF measurements in Figure 1.1.6, one sees that at times t = 0ms and from 4.0 – 5.2ms, there is little observable chemiluminescence signal from the OH* radical. As OH* is produced in the heat-release reactions of a flame, this lack of OH* signal indicates there is no strong heat-release zone present in the combustion chamber at this point of the cycle. The significant levels of ground state hydroxyl observable in the OH-PLIF images at the corresponding times indicate the presence of high-temperature burned gas, at least in first 40mm downstream of the burner face (corresponding to the OH-PLIF system field of view). From t = 0.8 – 3.2ms, one observes significant levels of OH* signal, indicating the presence of heat-release reactions. These images clearly show the roll-up, combustion and burn-out of the reactant pocket observed in Figure 1.1.6.

Figure 1.1.8 shows the corresponding velocity fields measured for the sequence above. Note that the field of view of the PIV imaging system is the same length (in the axial direction) as the PLIF measurement, but smaller in the radial direction. Therefore, to better capture the shear-layer dynamics, it is offset with respect to the burner centerline (toward the upper side of the combustion chamber). At time t = 0ms, one observes in the middle row (velocity magnitude) the vortex associated with the mushroom-shaped structure noted previously. This vortex is clearly associated with a high axial-velocity influx from the reactant channel pushing into virtually stagnant flow. As the reactant inflow enters the combustion chamber, a recirculation bubble forms downstream of the bluff-body and strengthens until approximately t = 2.4ms, after which the bubble collapses and the flow becomes stagnant. At the same time, the flame is observed to pinch off from the bluff-body and move downstream. A close inspection of the axial velocity fields in the bottom row confirms a small amount of the non-reacting hot gas enters the reactant channel upstream of the dump plane. Despite the relatively minor amount of upstream recirculation (based on very low velocity magnitude), it appears sufficient to sustain the thermoacoustic pulsation cycle in the burner.

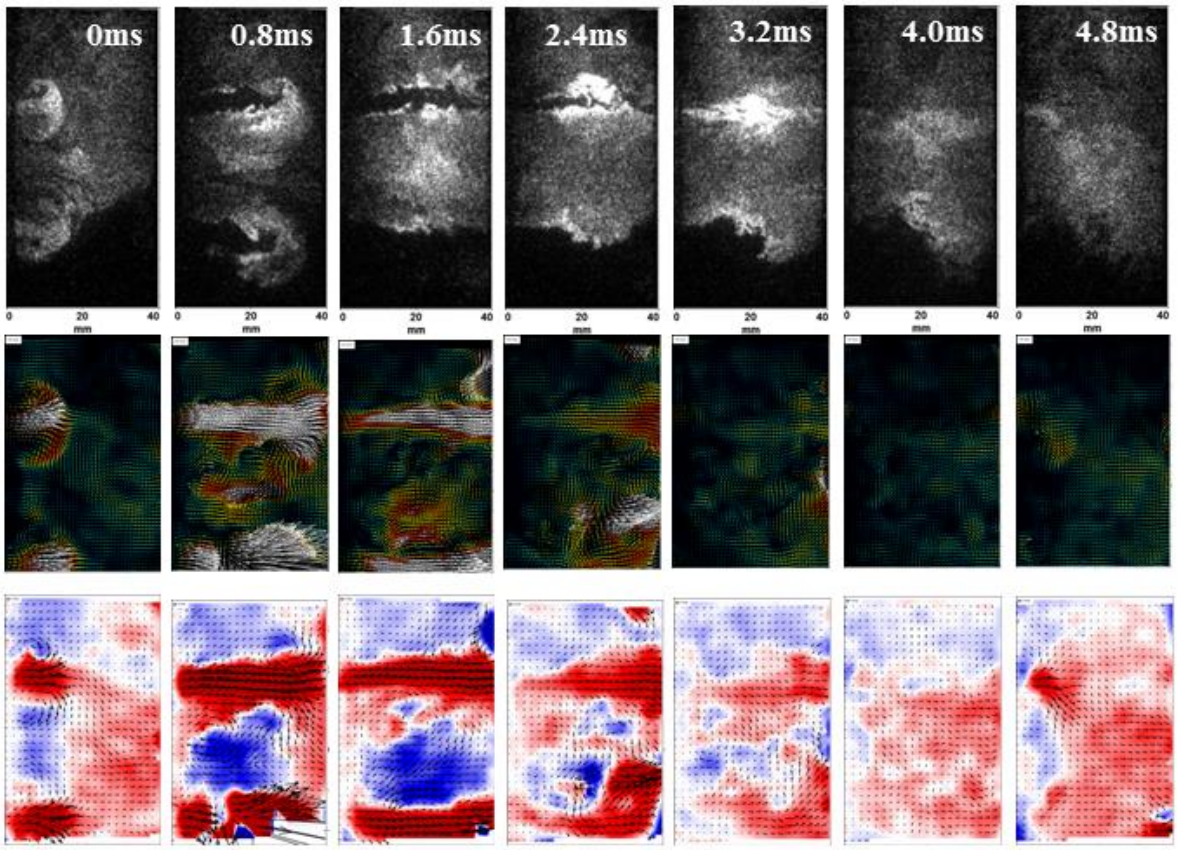

Figure 1.1.8. OH-PLIF (*upper*), velocity field magnitude (*middle*) and axial velocity (lower) fields acquired at flame condition "1i" (P = 3 bars, U_r = 20.6m/s, T_r = 423K, Phi = 0.67).

Taken together, Figures 1.1.6 - 1.1.8 suggest the strong, self-excited thermoacoustic pulsation is the overwhelmingly dominant characteristic of this flame. This pulsation induces a strong fluctuation in the reactant stream at the nozzle, resulting the periodic pinch-off and burnout of fresh reactants downstream of the burner face. This results in the periodic extinction of the reaction zone at the burner face but leaves sufficient hot, burned gas there to ignite the incoming reactants on the next cycle. The influx of hot products from the quasi-stagnant flow in the last quarter of the cycle appears to play a role in completing the acoustic feedback loop.

The DLR premixed bluff body burner was designed with geometry similar to that of the burner described in Balachandran et al., (2005). Although that burner has a substantially different confinement chamber, in that it exhausts directly to the atmosphere without passing through a convergent nozzle or back-pressure valve, it is nonetheless instructive to compare its dynamics to those observed in the DLR burner. Figure 1.1.9 is an image sequence reproduced from Balachandran et al., (2005) for the purposes of this comparison. It shows the flame surface density (FSD) measured via OH-PLIF at atmospheric pressure in a strongly forced flame in that burner.

Although the fuel, equivalence ratio and chamber pressure are significantly different, there are clear similarities between the dynamics of the flames in Figure 1.1.9 and those generated in the DLR burner, as well as some significant differences. For example, the roll-up and downstream propagation of a mushroom-shaped vertical structure at phase angle 80 – 240 degrees clearly resembles that observed in Figure 1.1.6. A key difference, however, is that this structure does not appear to induce pinch-off and downstream burnout of reactants in the Balachandran et al. (2005) measurements, as seen in the DLR burner. In addition, the presence of significant amounts of OH-signal within the mushroom shaped structure observed in Figure 1.1.6 indicates the presence of burned gas (and perhaps even combustion) upstream of the bluff-body during the course of the oscillation. This does not appear to be the case in the Balachandran et al. (2005) measurements. Nonetheless, the clear similarity between the flame shape and dynamics of the two burners suggests flames in the DLR burner

represent an extreme, limit-cycle behavior of the dynamics observed previously at atmospheric pressure in a burner of similar design.

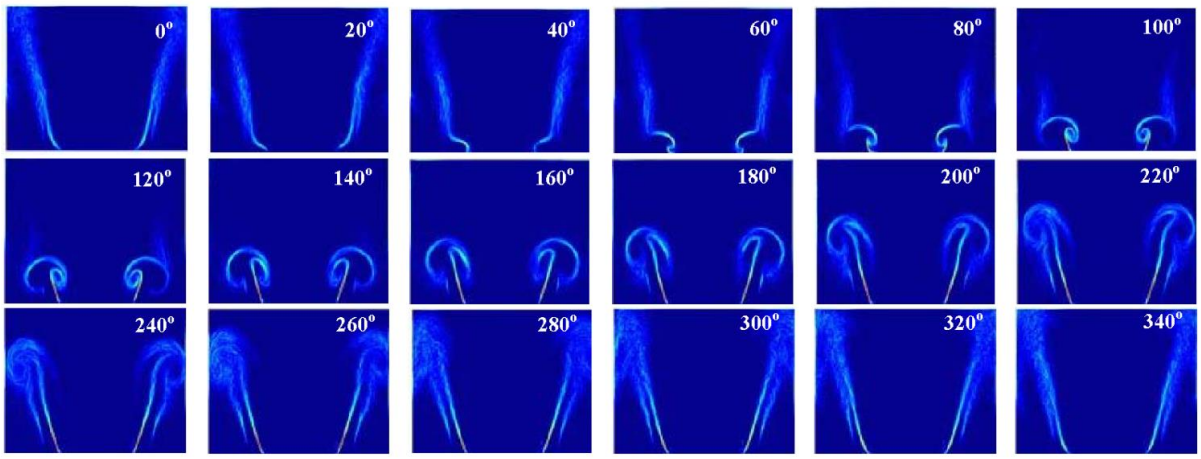

Figure 1.1.9. Phase-averaged FSD image sequence under strong acoustic forcing, measured in a bluff body burner of similar design, U_r = 9.9m/s, *f* = 160Hz, phi = 0.51. ***Reproduced from Balachandran, et al. (2005)***

Figure 1.1.10 shows the ensemble average of OH* chemiluminescence, OH-PLIF and axial velocity measurements acquired for Flame Condition 1i. Consistent with the image sequences shown in Figures 1.1.6 - 1.1.7, the mean images indicate that most of the heat-release in the flame takes place well downstream of the bluff-body face. In addition, note that mean OH* field shows a quite flat radial profile near the end of the flame, at approximately 60 – 70mm downstream of the exit. This is consistent with a flame that burns in the manner suggested by the discussion above, with most of the reactions taking place within a strong, propagating vortex shed from the rim of the bluff body. This explains the prevalence of OH* signal across the burner centerline well downstream of the burner face, rather than exclusively in and around the shear layers on either side of it.

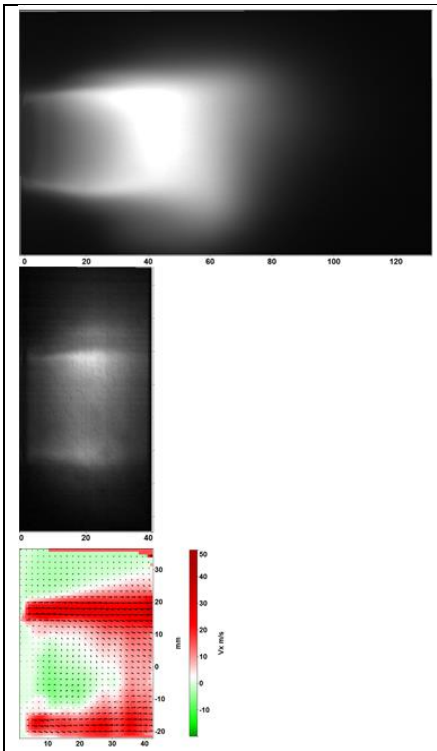

Figure 1.1.10 – Ensemble average of OH* chemiluminescence (upper), OH-PLIF signal (middle) and axial velocity (lower) measured at Flame Condition "1i" (P = 3 bars, U _r = 20.6m/s, T_r = 423K, Phi = 0.67).

The mean axial velocity field shown in the lower frame of Figure 1.1.10 is consistent with expectations for a bluff-body stabilized flame, with a recirculation zone extending from the bluff body to approximately 25mm (one diameter) downstream. This mean field is, however, misleading inasmuch as it suggests the continuous presence of a recirculation zone near the bluff body. The time-resolved axial velocity measurements presented in Figure 1.1.7 show this is certainly not the case. While hot gases are present near the bluff-body across the entire cycle of oscillation, the presence of a recirculation bubble in the same region is not. Rather, the recirculation bubble forms and collapses across the cycle.

To better understand the dynamics of the thermoacoustic instability, we phase-averaged the measurements with respect to the dominant thermoacoustic instability. A sample of these phase-averaged measurements is shown in Figure 1.1.11. The flames in this figure were measured at Conditions 1C and 1F. To the left side of each column are shown the points on the acoustic and heat-release cycles where each phase average was acquired. As expected, there appears to be a constant time-lag between the two. The phase averaged velocity and OH* fields indicate that the image sequence shown in Figures 1.1.6 – 1.1.7 are truly representative of the flame dynamics.

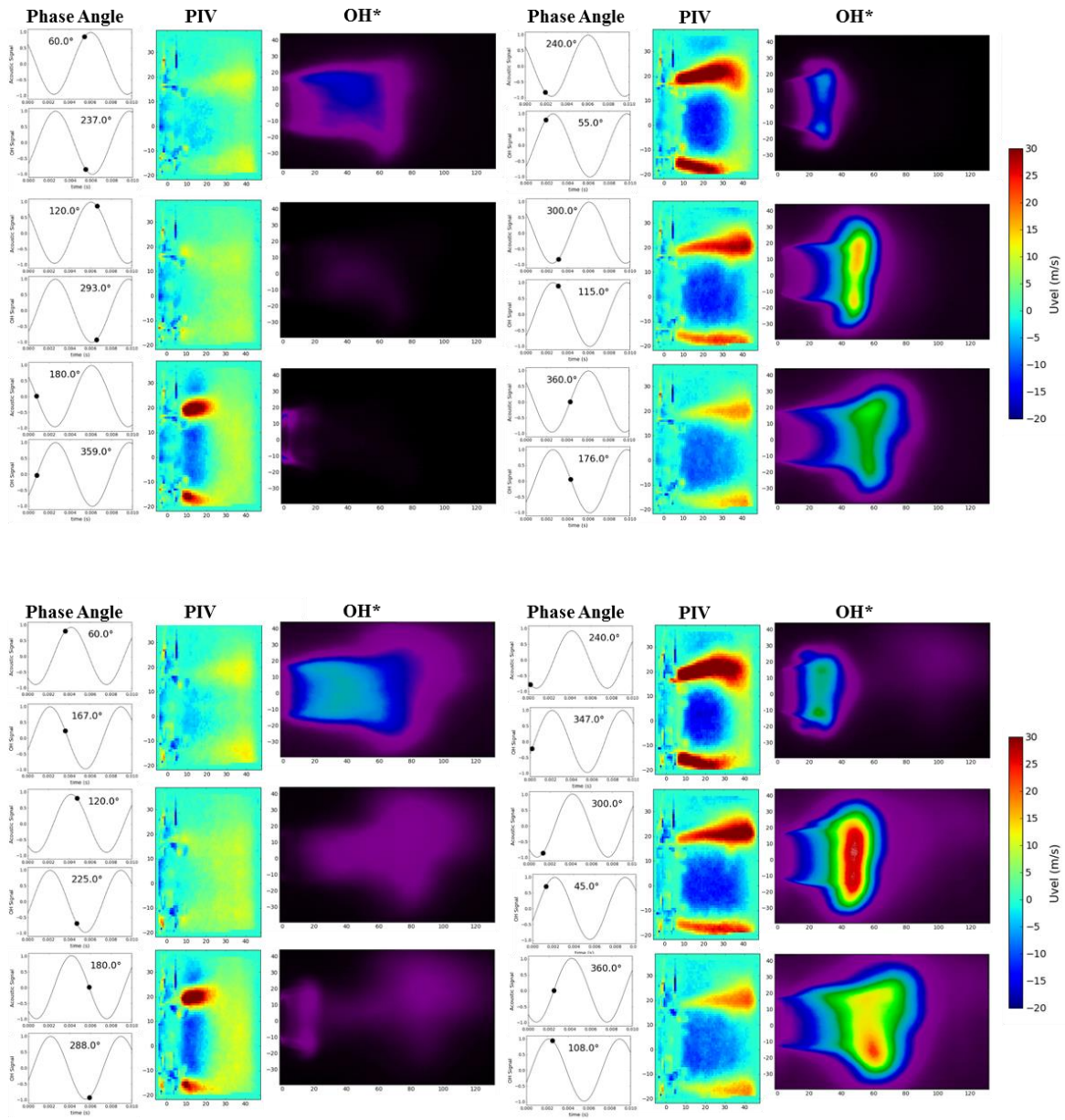

Figure 1.1.11. - Phase-averaged PIV and OH* measurements of flames measured at Condition 1c (upper) and 1F (lower). This corresponds to P = 3 bars, U = 10.1m/s and ϕ = 0.77 and 1.0, respectively.

Analysis of this data set is ongoing at the time of writing. Initial findings from this series of measurements have been accepted for publication in scientific and technical conferences including the 29. Deutscher Flamentag and the ASME Turbo Expo 2020.

Measurement Series 2 – Pressure Effects

The goal of the second measurement series was to test and characterize the viability of high bandwidth laser imaging measurement of turbulent flames at increasing chamber pressure. The flame conditions targeted in this series are outlined in Table 2. Before analyzing the performance of the OH-PLIF system however, it is useful to characterize the target flames themselves.

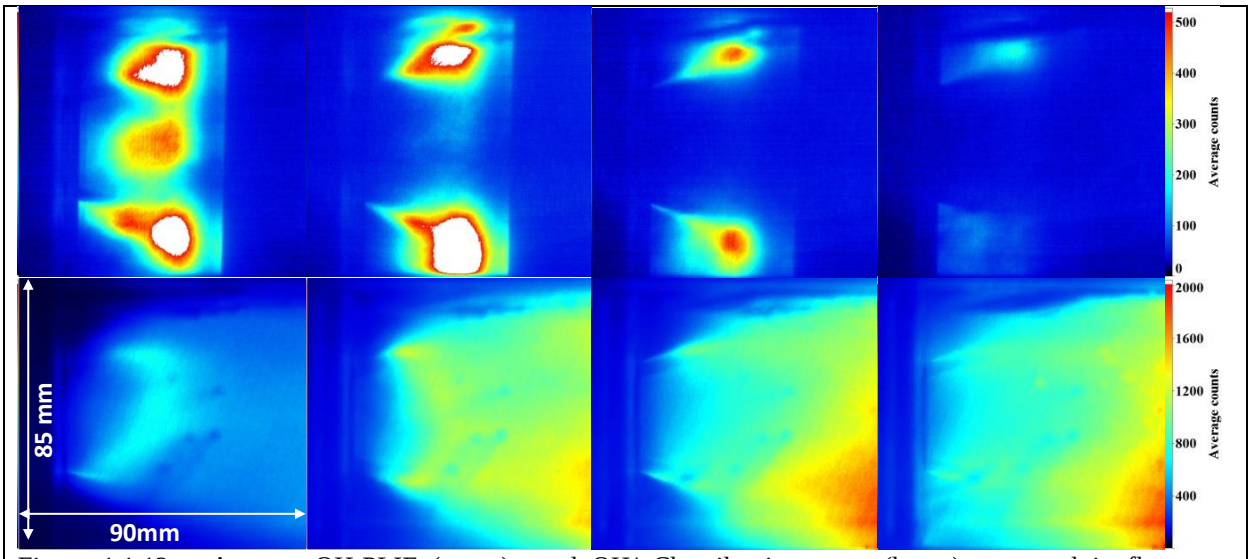

Figure 1.1.12 – Average OH-PLIF (upper) and OH*-Chemiluminescence (lower) measured in flames at Conditions 2b, 2c, 2h and 2m, which correspond to 5, 10, 15, and 20 bars. Flow is from left to right.

Figure 1.1.12 shows ensemble-averages of the OH*-chemiluminescence and OH-PLIF images acquired at several flame conditions studied in measurement series two. Flow in these images is from left to right. The conditions shown are described in Table 2 as cases 2b, -c, -h and -m, respectively and correspond to chamber pressures of 5, 10, 15 and 20 bars. The same color map is used for all four mean OH* images, illustrating the increasing OH* signal levels observed with increasing chamber pressure. Similarly, the same color map is used for all four mean OH-PLIF images, illustrating the significant drop-off in OH signal intensity with increasing chamber pressure. This is consistent with previous observations. Understanding how this affects the viability of highspeed OH-PLIF measurements was a key motivation for this study.

The mean images shown in Figure 1.1.12 reveal several important features of the flames in measurement series two. Key amongst these is that at pressures above 5 bars the flame appears to stabilize primarily in the outer shear-layer of the burner. That is, the flame appears to stabilize in the shear layer originating at the outer circumference of the reactant inflow channel. This is evident from the strong, single interface of high OH-PLIF signal magnitude observed outside the wake region of the bluff-body and minimal observable signal at the edge of the bluff-body itself. The mean OH* images suggest a weaker (in the mean) flame exists on the inner shear-layer.

The fact that the flame appears to stabilize in the outer shear-layer was unexpected, given that the burner was designed to stabilize a flame in the wake of a bluff-body. The reason for this unexpected stabilization mechanism lies in the dynamics of the flame. Although not immediately clear from the mean images, but consistent with the flames in measurement series 1, the flames in measurement series two showed strong, self-excited thermoacoustic pulsation. The axial motion associated with this "puffing" phenomenon leads to spatial "smearing" of the time-averaged OH* and OH-PLIF signal on the burner centerline. The OH signal (both PLIF and self-excited chemiluminescence) in the outer shear layer remained mostly in the same position throughout the cycle. This was likely due to the confinement effect of the wall.

Figure 1.1.12 demonstrates a critical achievement of this project to date. It is (to the authors' knowledge) the first time OH-PLIF measurements have been acquired at 10 kHz in turbulent, premixed flames at 20 bars pressure. Despite the very low signal intensity achieved at this pressure, this is clearly an important milestone in the project.

To help better understand the effect of thermoacoustic pulsation on the flames studied in measurement series two, Figure 1.1.13 shows a series of OH* image sequences acquired at the flame conditions shown in Fig. 1.1.12. In this figure, flow is from left to right and time separation between each image is 2ms (i.e. every twentieth frame acquired during an imaging run). Images in the first, second, third and fourth row were acquired at flame conditions 2b, -c, -h and -m, respectively and correspond to chamber pressures of 5, 10, 15 and 20 bars. The color map is the same for all four image sequences, to illustrate the increasing OH* signal levels observed with increasing chamber pressure.

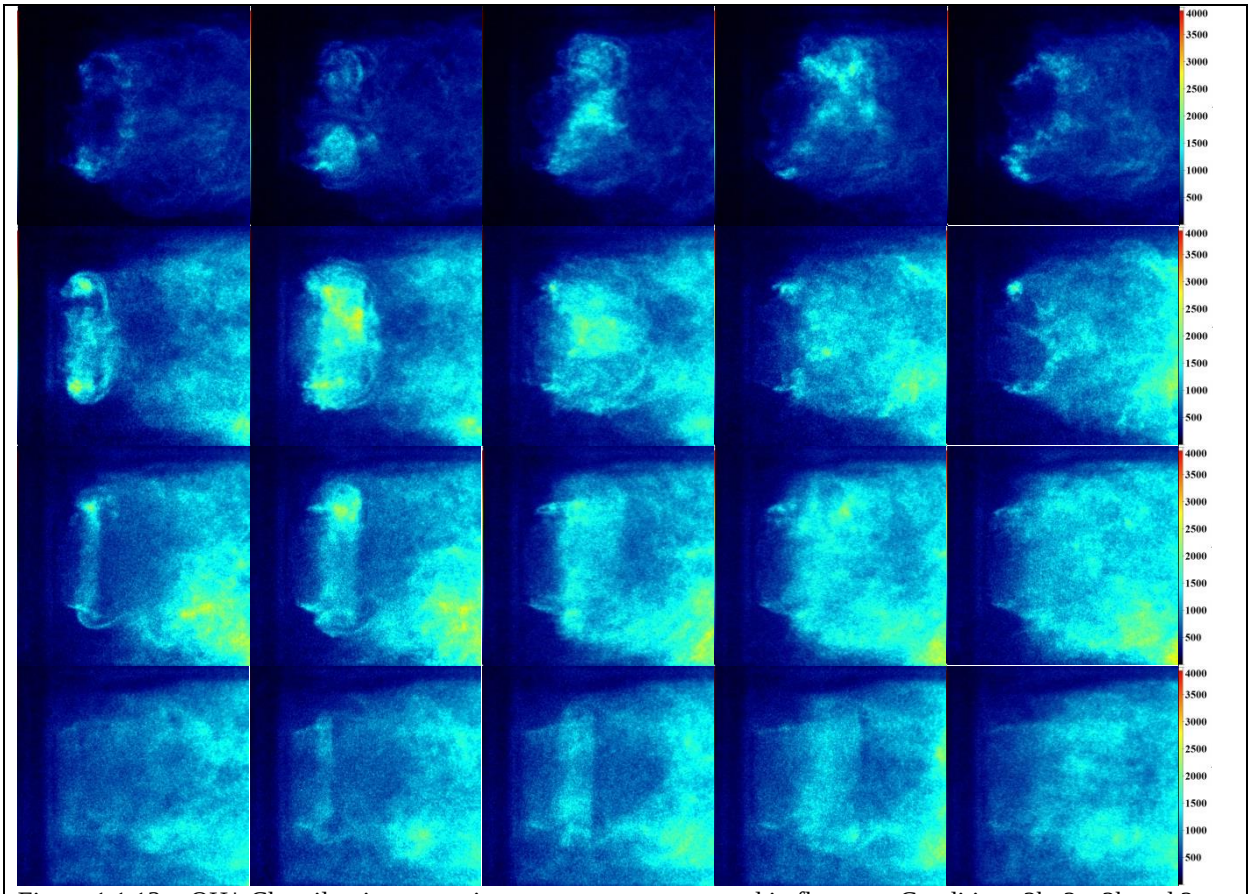

Figure 1.1.13 - OH*-Chemiluminescence image sequences measured in flames at Conditions 2b, 2c, 2h and 2m, which correspond to 5, 10, 15, and 20 bars. Flow is from left to right. Time between frames is 2ms.

Row 1 shows images acquired over a period corresponding to approximately one cycle of the 150Hz oscillation observed at this condition. Visible in the first frame of this sequence is a roll-up of the flame sheet near the outer circumference of the reactant inflow channel. This roll-up is clearly associated with the propagation of a shear-layer vortex from the bluff-body injector. In subsequent frames one observes this disturbance propagate downstream and grow in size, as one would expect for a vortex-flame interaction like this. A similarly strong vortex-flame interaction is observable in the other sequences, albeit somewhat obscured by the higher intensity background signal levels.

Consistent with the flames in measurement series one, analysis of both the OH* image sequences, PIV and acoustic measurements reveal a very strong coupling between the shear layer and flame in this burner and that this is, in turn, coupled with the measured thermoacoustic pulsation. The frequencies and intensity of this pulsation were observed to vary somewhat with pressure but at all conditions, the flame was found to exist only at conditions of limit-cycle thermoacoustic pulsation. Although flames in a state of limit-cycle thermoacoustic oscillation are usually not desirable in a technical burner, these flames imaged in measurement sequence two are intended purely as imaging targets for the high bandwidth laser imaging system and represent a viable test case for the project.

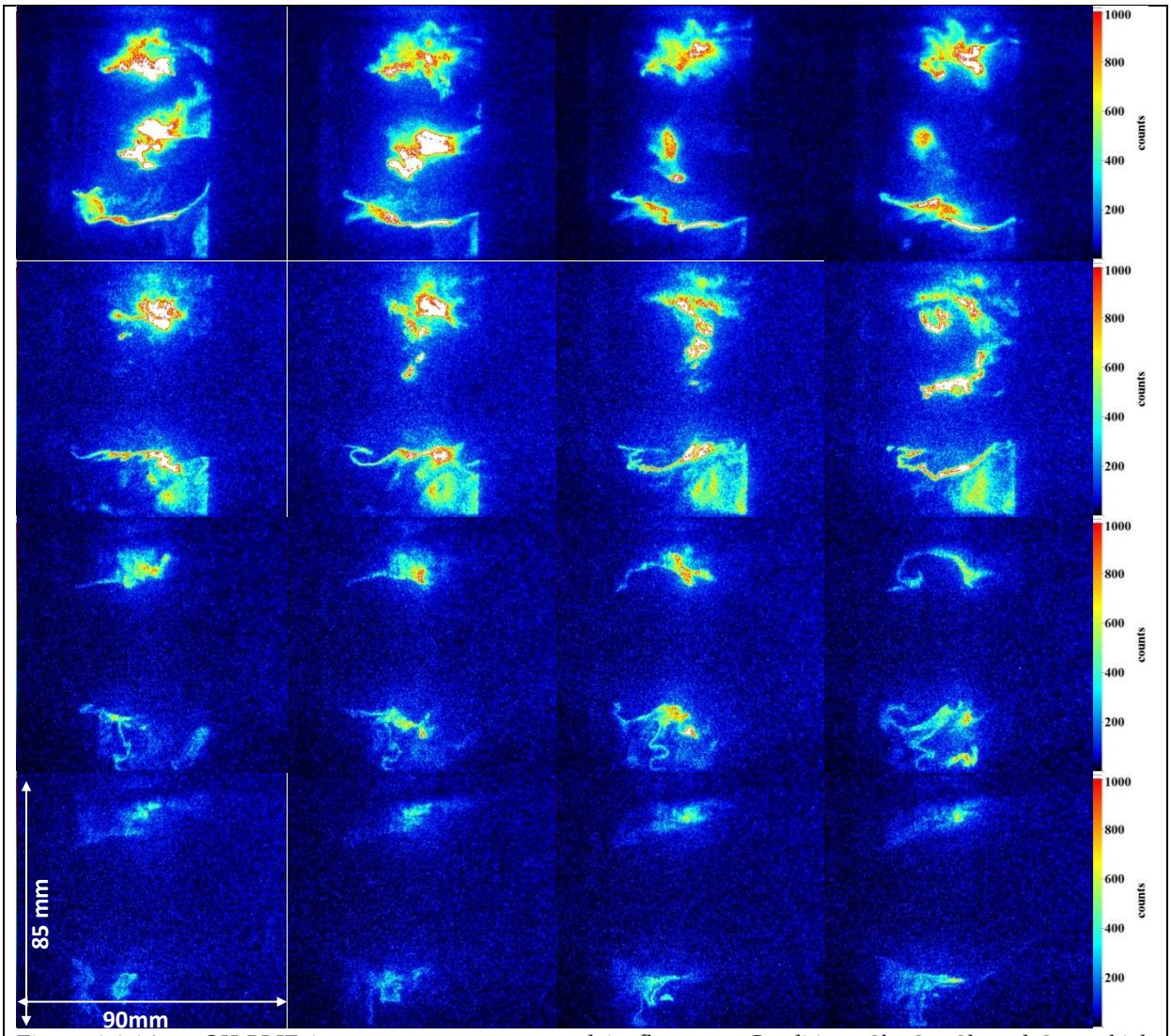

Figure 1.1.14 - OH-PLIF image sequences measured in flames at Conditions 2b, 2c, 2h and 2m, which correspond to 5, 10, 15, and 20 bars. Flow is from left to right. Time between frames is 2ms.

Figure 1.1.14 shows a series of OH-PLIF acquired at the same flame conditions displayed in Figure 1.1.13. This image shows the strong pressure dependence of OH-PLIF signal levels. Whereas in the first two rows, at P = 5 bars and 10 bars respectively, the reaction zones of the flame are clear and easily distinguishable from the background, those in the latter two rows are challenging to distinguish from background noise.

Figure 1.1.14 illustrates the strong pressure dependence of the OH-PLIF signal-to-noise ratio. The images in Row 1, acquired at 5 bars chamber pressure show almost an order of magnitude greater SNR than those in Row 4, which were acquired at 20 bars chamber pressure. Figure 1.1.15 shows the mean SNR for the OH-PLIF measurements acquired at 5, 10, 15 and 20 bars pressure. They decrease almost linearly from approximately 30 down to approximately 5. Of course, mean SNR is only one measure of interest in determining the viability of high bandwidth laser imaging measurements but is indicative of the challenge associated with this technique.

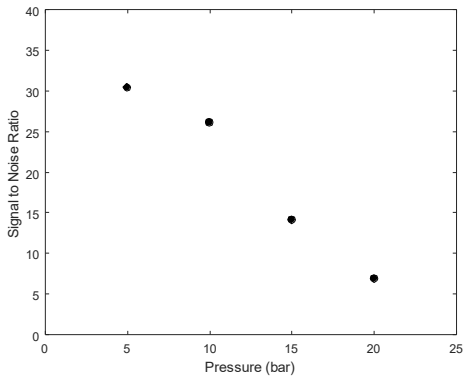

Figure 1.1.15 – Signal-to-Noise ratio of mean OH-PLIF images vs chamber pressure.

Section 1.2 – High bandwidth laser imaging measurements of turbulent, swirl-stabilized flames at elevated pressure conditions

Introduction / Background

The work plan for this project called for the deployment of the highspeed laser imaging diagnostics developed in Phase 1 to rigorously characterize the flow-field and flow-flame interaction of lean, turbulent swirl flames at elevated pressure conditions. This objective was achieved during the course of several measurement campaigns completed at the German Aerospace Center in Stuttgart. These measurement campaigns were split into three series; Series A and B, which were completed a smaller, (tabletop scale) high pressure test facility and Series C, completed in the larger (300kW class) HIPOT test rig.

The reason for splitting the measurements between two different testrigs was primarily a practical one. It was far more cost effective and easier to schedule facility time in the smaller test rig than in the larger one. The injector geometry in both cases was similar, as were the overall combustor dynamics. The key difference was higher overall chamber pressure reachable in the HIPOT. Despite this minor modification to the original plan of completing all measurements in the HIPOT test rig, it is fair to say the goals for this part of the project were successfully achieved. The measurement campaigns and key findings of each are described (separately) below.

Measurement Series A

The goals of this experiment (Measurement Series A, or "MS-A") were to 1) explore the effect of radial air staging on the flowfield dynamics of a gas turbine model combustor at elevated pressure conditions and 2) develop wavelet-based signal processing tools for the analysis of the large data sets of the sort generated in this project. The first measurement campaign of MS-A was completed in April, 2016 during a site visit by AFRL researcher, Dr. Campbell Carter. Dr. Carter's visit was supported through the AFOSR "Windows on the World" program. The development and application of Wavelet-based analysis techniques was completed through an unfunded collaboration with Professors Jacques Lewalle and Ben-Akih Kumgeh of Syracuse University.

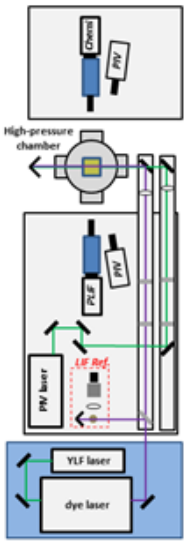

Figure 1.2.1 –Apparatus used in Measurement Series A

Burner and Flame Condition

The burner used in this study is described in refs. [2-4]. It consists of a swirled fuel-air injector and an optically accessible combustion chamber. It is mounted in an optically accessible pressure vessel. The injector consists of two coaxial air nozzles, separated by a ring of fuel-injection channels. The inner air nozzle measures 12.3 mm in diameter. The outer (annular) air nozzle has an inner and outer diameter of 14.4 and 19.8 mm, respectively. Dry air for each nozzle is supplied separately, via electromechanical flow controllers (Bronkhorst). Swirl is induced in the flow through each nozzle via a set of radial swirl vanes. Gaseous fuel (C_2H_4, also set via Bronkhorst flow controllers) is injected via a ring of 60 straight channels (0.5×0.4 mm^2) located between the inner and outer nozzles. The exit planes of both the fuel and the air flows are located at the level of the combustion chamber inlet, ensuring maximal optical access to flame dynamics at the nozzle exit.

The combustion chamber measures 120 mm in height and has a square cross-section measuring 68 × 68 mm^2. It has four fused silica windows (127 mm × 59 mm × 3 mm), yielding an optically-accessible area of 51.4 mm × 120 mm. This chamber is mounted in a water-cooled stainless steel pressure vessel with four large windows for optical access (60 × 120 mm^2). The chamber pressure is adjusted via a movable piston back-pressuring valve.

Flames were measured at 12 operating points in this study. Conditions 1-11 were designed to identify the effect of radial air staging on a swirl-stabilized flame at constant stoichiometry, chamber pressure and bulk flow velocity. In these cases, the ethylene-fueled flame was operated at (global) $\Phi = 0.67$, thermal load of 33kW and chamber pressure of 5 bars. In these cases, radial air staging (defined as the percentage of total air flow delivered via the central, radially-swirled injector nozzle) was varied from 0 – 100% in increments of 10%. At condition 12, the burner was operated at a chamber pressure of 5 bars to produce a flame with equivalence ratio of 0.91 and thermal power of 54.2 kW. At this condition, the combustor experiences frequent spontaneous transitions between stable- and thermoacoustically excited operational states, making it an ideal test-case for the wavelet-based pattern recognition algorithms developed in this project.

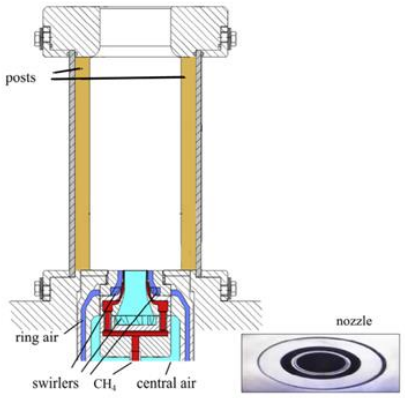

Figure 1.2.2 – Dual-swirl gas turbine model combustor

Measurement Apparatus

The measurement apparatus used in this study consisted of a kHz acquisition-rate stereoscopic PIV system, a kHz acquisition-rate OH-PLIF system, a kHz acquisition-rate OH* chemiluminescence imaging system, a kHz acquisition-rate OH-PLIF system and a fast-response piezoresistive pressure transducer.

Stereo-PIV System

The stereoscopic PIV system consisted of a dual-cavity, diode-pumped, solid-state Nd:YAG laser (Edgewave, IS200-2-LD) and a pair of CMOS cameras (2 × LaVision HSS8). The laser produces up to 9mJ/pulse at 532 nm at repetition rates up to 10 kHz and with pulse durations of 14 ns. The beam was formed into a laser sheet using a cylindrical telescope. Mie scattering from titanium dioxide (TiO_2) particles (nominal diameter 0.5 μm) seeded into the air flow of each nozzle was imaged using a pair of CMOS cameras. The cameras were mounted on opposite sides of the laser sheet and had sufficient on-board memory (32 GB) for up to 3.8 seconds of dual-frame PIV imaging at 9.3 kHz and 512 × 640 pixel resolution. The cameras were equipped with 100-mm focal length, f/2.8 objectives and were mounted on custom rotation fixtures and Scheimpflug adaptors. The spatial resolution of the system was 2 mm, based on the size of the PIV interrogation region (24 × 24 pixels).

Planar Laser-Induced Fluorescence

The OH-PLIF system consists of a conventional (albeit modified) frequency-doubled dye laser and an intensified CMOS camera. The dye laser (Sirah Cobra-Stretch HRR, using Rhodamine 6G in ethanol) was pumped with a frequency-doubled, Q-switched, diode-pumped solid state Nd:YLF laser (Edgewave IS-811E). At 3.1 kHz, the time-average output from the dye laser at 283.9 nm was ≈ 0.7 W or 225 μJ/pulse. The laser line width at 566 nm was 0.06 cm^{-1} while that of the frequency doubled output was ≈0.09 cm^{-1}. Wavelength tuning of the dye laser to the overlapped $Q_2(8)$ and $Q_1(9)$ lines of the A-X (1,0) band of OH was monitored continuously using a setup consisting of a laminar reference flame and a photomultiplier tube for fluorescence detection.

The 283-nm beam was formed into a sheet of ≈40 mm (high in the probe region) using two fused silica lenses (f_{plif1} = -50 mm, f_{plif2} = 150 mm) in a cylindrical telescope configuration and focused to a waist using a third cylindrical lens (f_{plif3} = 750 mm). The 283-nm laser sheet was overlapped with the PIV laser sheet using a pair of dichroic mirrors (see Fig. 1). The PIV and PLIF sheets were overlapped in the near and far fields and also in the probe region; this process was checked daily, and the overlap was found to be consistently very good.

Fluorescence signal was acquired with a CMOS camera (LaVision HSS6), external two-stage, lens-coupled intensifier (LaVision HS-IRO) and a fast Cerco 100 mm, f/2.8 lens that is AR (anti-reflection) coated for the UV. Background luminosity was reduced using a 100-ns intensifier gate, and elastic (particle) scattering at 283 nm was blocked using a high-transmission (> 80% at 310 nm) bandpass interference filter (Laser Components GmbH).

OH Chemiluminescence Imaging System*

Chemiluminescence from the electronically excited OH* radical was imaged using a high-speed CMOS camera (LaVision HSS6) and external, two-stage, lens-coupled intensifier (LaVision HS-IRO) with a 45 mm focal length, f/1.8 objective (Cerco) and the high-transmission, band-pass interference filter. The integration time of the intensified camera was 5 µs. The camera was operated at 512×512 pixels resolution and 3.1-kHz acquisition rate, with 8192 images (2.64 s) being acquired per imaging run.

Acoustic Measurement System

The acoustic measurement system consisted of a piezoresistive pressure transducer (Kistler 4045A20) with a natural frequency of 150 kHz and a measurement range of 0 – 20 bars, connected to a (Kistler Type 4603A) amplifier. The transducer was mounted (via a calibrated probe) to the exhaust plate of the combustion chamber. The transducer signal was read into a digital recording oscilloscope (a LeCroy HDO 6054 with 500-MHz bandwidth and 12-bit resolution ADC). The oscilloscope was used to record both the pressure transducer signal and a trigger signal from the high bandwidth imaging system. This trigger signal was used to synchronize the acoustic signal to that of the PIV, PLIF and OH* images.

Results and Discussion

Air Staging

Figure 1.2.3 shows the mean velocity field for the reacting and non-reacting flow at each of the eleven flow conditions measured in MS-A. In this figure, the background color contours represent the magnitude of axial velocity. The vectors show total velocity magnitude and direction. For clarity, only every second vector is plotted. The upper and lower plot in each sub-figure represents the non-reacting and the reacting flow field, respectively. The trends revealed by these sub-figures are discussed (separately) below.

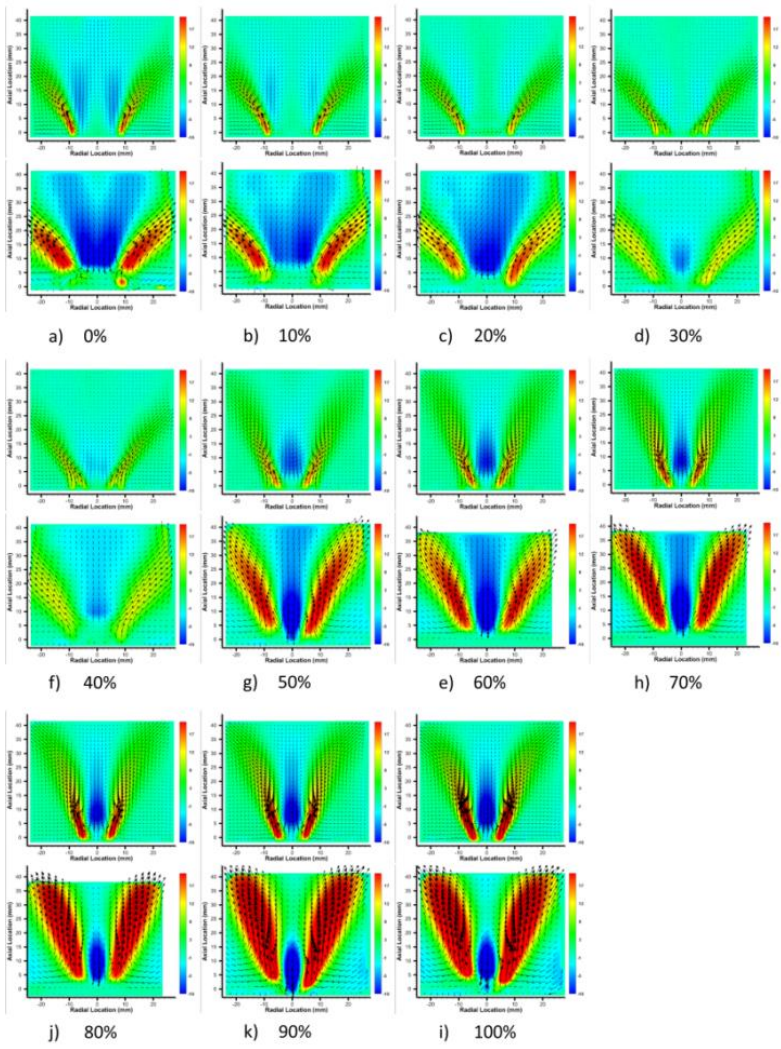

Figure 1.2.3 – Mean flow fields for the nonreacting (upper) and reacting (lower) flow conditions at each air staging.

Figure 1.2.3 illustrates a clear trend in the velocity field of the non-reacting flows as one changes the air split ratio. In Figure 1.2.3, where no air issues through the center nozzle (i.e. 0% air split), the mean flow field shows a conical inflow of reactants, with a stagnation region near the burner centerline. Downstream of this stagnation region one sees apparently separate recirculation bubbles aligned with the shear layers. These recirculation bubbles grow with axial distance from the nozzle and coalesce into a single recirculation zone approximately 30mm downstream. As the flow is axisymmetric in the mean,

Figure 1.2.3 is likely illustrative of a stretched toroidal recirculation bubble. With increasing air split, the mean velocity gradient across the inner shear-layer decreases (and with it, the shear) causing these recirculation bubbles to weaken and eventually disappear. This trend culminates at an air split of 30%, where one sees only very weak recirculation bubbles on the inner shear-layer, and these coalesce almost immediately. Beginning at air split of 40%, one observes a single contiguous recirculation zone in the non-reacting flow field. This recirculation zone becomes stronger with increasing air splits and the opening angle of the incoming reactant flow becomes narrower. Consistent with conservation of mass, the peak mean velocity of the reactants increases as more air is put through the (smaller) central nozzle.

Comparing the flow fields of the reacting and non-reacting flow reveals both similarities and important differences. The region of high velocity reactant inflow shows a similar trend in both cases, with opening angle starting out wide and then narrowing with increasing air split. The reacting flow data shows a significantly slower velocity-decay in the reactants than does the non-reacting flow. This may reflect flow blockage in the combustor resulting from volumetric expansion driven by heat release or decreased turbulent mixing along the shear-layer resulting from the presence of a flame.

The key difference between the mean velocity fields of the reacting and non-reacting flows is observed in the inner recirculation zone. Whereas the non-reacting data shows a stagnation region along the burner axis in the 0% air split condition, the reacting flow case shows strong recirculation, indeed possibly extending up into the inner swirl nozzle. Consistent with the non-reacting cases, this recirculation zone weakens with increasing air split. In contrast with the non-reacting cases however, which gradually increase in size and strength with increasing air split, the recirculation bubble in the reacting flow case strengthens dramatically between the 40 and 50% air split conditions and then remains approximately the same size and strength with increasing air split. This suggests a different physical mechanism drives the structure and dynamics of the inner recirculation zone in each case.

Peak Frequency in the IRZ

To better understand the mechanism responsible for the observed differences in the IRZ, a time-series of velocity vectors was extracted for each condition from a monitor point on the burner centerline, 5mm downstream of the nozzle exit. This time-series data was used to compute the frequency spectra of each component of velocity, as well as the total velocity magnitude. In all but two cases (non-reacting, with air splits of 0 and 10%), the velocity magnitude spectra showed strong peak oscillation frequencies.

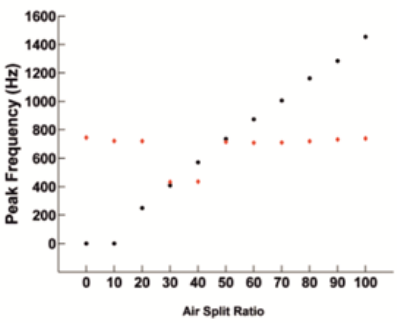

Figure 1.2.4 – Peak frequency measured at a monitor point on the axial centerline of the burner, 5mm downstream of the nozzle. Black dots represent the nonreacting flow, and red the reacting.

Figure 1.2.4 shows the peak oscillation frequency measured at each flow condition, with black circles representing non-reacting flow cases and the red diamonds for reacting flow. It is immediately clear from this plot that the dynamics of the recirculation zone are fundamentally different. Whereas the non-reacting flow shows a linear increase in peak oscillation frequency with increasing air split, the peak oscillation frequency of the reacting flow case remains virtually constant (≈ 720 Hz) regardless of air split, except for the case of 30/70 and 40/60, where it overlaps well with the peak frequency measured in the non-reacting flow cases.

It was observed previously that for the baseline (30/70 air split) test condition the dominant turbulent flow structure in the combustor is a helical vortex that precesses about the burner centerline at a frequency of 409-435 Hz. Comparing this to the peak frequency measured at the monitor point, it is clear that the dominant frequency measured in both the reacting and non-reacting flows at that condition is associated with the helical PVC. It is known from previous studies [5] that the precession frequency of the PVC scales with the bulk flow velocity. Given the strong correlation between peak frequency and air split in the non-reacting data, it is reasonable to conclude that the helical PVC is the dominant turbulent flow structure in the burner for all non-reacting flow cases with air splits greater than 10%.

The peak oscillation frequency measured in the reacting flow cases is approximately 730 Hz for all air splits except 30 and 40%, where the mean velocity gradient between flows originating from the inner and the outer swirl nozzles is minimal. The same frequency was measured via a pressure transducer, indicating the peak oscillation frequency in those cases corresponds to the thermo-acoustic pulsation. This indicates that when self-excited thermoacoustic oscillation is present in the flame, it tends to dominate the dynamics of the inner recirculation zone. The onset of self-excited thermo-acoustic pulsation appears strongly linked with air staging in this burner.

To identify the effect of thermoacoustic pulsation on the flow-field, a POD was performed on the PIV data acquired at each air split. Figure 1.2.5 shows the first two (i.e. most energetic) eigenmodes of the PIV data for the flow condition with 50/50 air split. Also shown are the first 100 points of the time series of multiplicative constants associated with these eigenmodes. Consistent with the eigenmodes observed in the baseline case (30/70 air split), the eigenmodes in this case consist of a series of vortices aligned along the shear-layer of the incoming flow. Furthermore, the multiplicative constants oscillate at the same frequency, separated by a constant phase lag. In contrast with the baseline case (30/70 air split), the sign of the vorticity in this case is opposite on either side of the burner axis. The anti-symmetry in vorticity across the burner axis is consistent with ring-vortices being shed periodically from the injector nozzle. The fact that these vortices are shed at precisely the frequency of the self-excited thermoacoustic pulsation strongly suggests the two are coupled. It is unclear from the velocity data alone which phenomenon is responsible for this coupling. Nonetheless, is appears consistent in all cases except those with 30/70 and 40/60 air splits.

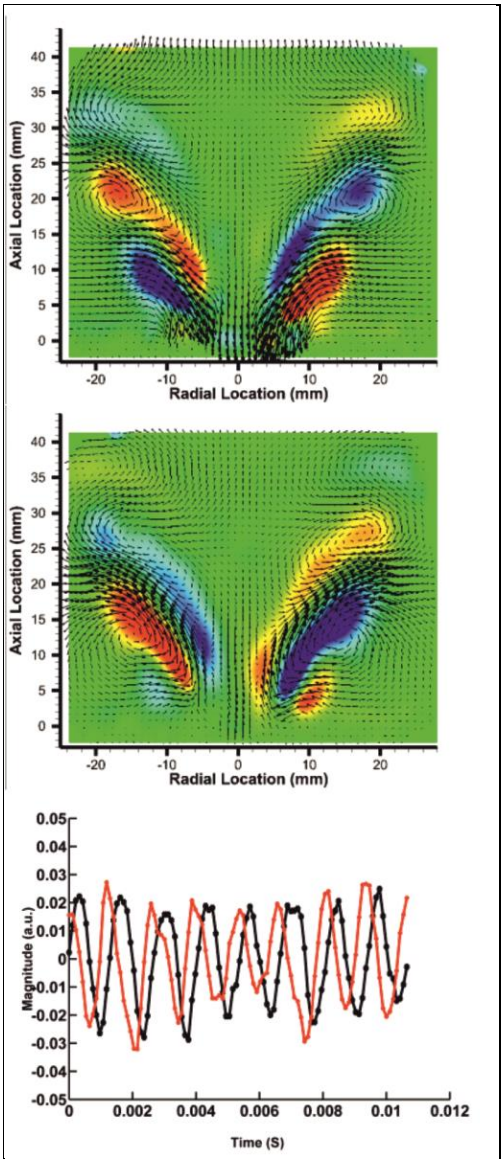

Figure 1.2.5 – The dominant eigenmodes measured in the reacting flow condition with 50/50 air split.

Flame Transitions

Figure 1.2.6 presents the measured time-series of a) acoustic pressure, b) OH* chemiluminescence (integrated over the entire image) and c) the fluctuating component (standard deviation) of axial velocity integrated over each measurement frame acquired at flame condition 12 (i.e. the case with spontaneous flame transitions). These plots clearly show a transition from a stable operation (having low pressure fluctuations) to an excited one (having strong pressure fluctuations). This transition occurs at approximately $t = 1.3$ *s* and results in a dramatic increase the magnitude of pressure and velocity fluctuations and an overall drop in OH* chemiluminescence signal. As OH* is a commonly accepted marker for heat release [6], the drop in signal may be interpreted as a corresponding drop in heat-release within the measurement window. As can be seen, the mean pressure in the combustor drifts from 5.1 bars to a slightly lower value following the transition before stabilizing at approximately t = 3.5s. This may be a result of the combustor and test-rig thermally equilibrating after the flame transition.

It is important to note the data presented in Figure 1.2.6 were acquired in a single measurement run and as such may not be broadly representative of the physics of stable-to-excited flame transitions. Indeed, even within the six long-duration measurement runs acquired in this study, a variety of transition phenomena were observed, including stable-to-excited, excited-to-stable and short-lived, intermittent jumps between stable and excited states. With that in mind, the dataset in Figure 1.2.6

serves as an excellent test case to investigate the strengths and limitations of wavelet-based signal analysis tools used in this study.

Before focusing on flow physics specific to the transition itself, it is useful to characterize the flow field and flame in the stable and excited states. Figure 1.2.7 presents ensemble averages of the measured data in the stable (left column) and in the excited (right column) states. The upper frames show the OH*-chemiluminescence signal, each averaged over 3100 frames (1-s measurement period). The lower frames show the measured velocity fields for each state, also averaged over 1s. The vectors indicate direction and magnitude of the velocity. The background contour displays the magnitude of the axial component of velocity.

Figure 1.2.7 reveals important similarities and differences between the flow fields of the flame in the stable and in the excited states. In both cases, the mean velocity fields consist (as expected for high-swirl flows) of a conical region of high velocity reactants, an inner recirculation zone (IRZ) and an outer recirculation zone (ORZ). The IRZ results from vortex breakdown in the highly swirling reactant inflow and serves to stabilize the flame by transporting hot combustion products and combustion radicals back toward the dump plane, where they mix with incoming reactants and thereby increase reactivity and flame speed. The ORZ results from the confinement chamber surrounding the injector.

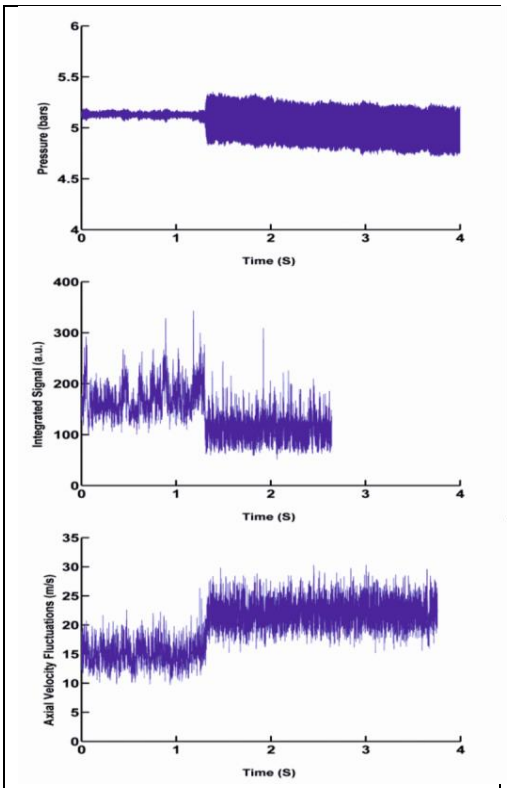

Figure 1.2.6 – Time-series measurements of a) Acoustic pressure, b) OH* Chemiluminescence and c) r.m.s. axial velocity fluctuations in the combustor.

Figure 1.2.7 also shows the flow-fields have similar opening angles for the region of high-velocity reactants. In the stable condition, however, the flow-field has a significantly higher rate of velocity decay vs. downstream distance and a much weaker inner recirculation zone. This is consistent with previous research, which has shown that thermo-acoustic oscillation in this burner is accompanied by a strong fluctuation in axial velocity along the centerline. This oscillation severely affects the stability of the shear-layer and interrupts the recirculation of hot combustion products to the base of the flame. It also has the effect of i) increasing mean velocity of the flow impinging at the combustor wall and ii) increasing the strength of the ORZ.

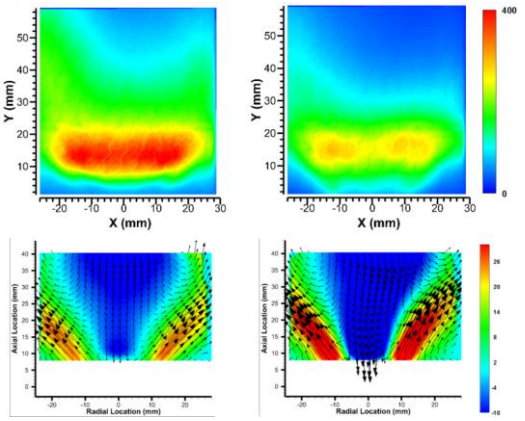

Figure 1.2.7 Mean OH* chemiluminescence (upper) and axial velocity (lower) fields. The left and right columns correspond to the flame in the stable- and the excited state, respectively

A useful tool for identifying transient phenomena associated with unpredictable events like stable-to-excited transitions in a swirl flame is the wavelet transform. In this study, we apply the continuous wavelet transform to "zoom in" on frequency content of the signal around the time of the stable-to-excited transition. Thorough presentations on continuous wavelets can be found in refs. [8,9]. The wavelet transform is the convolution of the wavelet with the signal u(t):

$$\tilde{u}(f,t) = \int_{-\infty}^{\infty} u(t')\psi^*(f, t-t')dt'$$

The plot of this function's contour lines in a time-frequency domain is called a scalogram; its value at a particular time and frequency is a wavelet coefficient. Denoting the Fourier transform by

$$\hat{u}(f) = \int u(t) \exp(-2i\pi ft) dt$$

the wavelet transform can also be expressed as a band-pass filtered signal, with the wavelet determining the shape of the frequency band, since

$$\tilde{u}(f,t) = \int \hat{u}(\omega) \hat{\psi}^*(\frac{\omega}{f}) \exp(2i\pi\omega t) \, \mathrm{d}\omega \ .$$

The norm of the Morlet coefficients can be interpreted as the envelope of the fluctuations at a given frequency, and the real part is a representation of the fluctuations inside the envelope.

Figure 1.2.8 (reproduced from ref. [9]) shows the envelope scalogram of the axial velocity field measured during a 0.4-s period straddling the transition from the stable to the excited state. The horizontal and vertical axes represent time and frequency, respectively. Darker shades correspond to more energetic fluctuations. The dominant oscillation frequencies described above are highlighted on this plot via colored lines. Scalograms were also computed for the acoustic- and OH*-chemiluminescence data and showed consistent activity within each frequency range. Of particular interest in Figure 1.2.8 is the presence of a short-lived, 635-Hz oscillation in the signal that appears at $t \approx 1.15$ s and persists until $t \approx 1.3$ s, when the 720 Hz thermoacoustic oscillation appears and becomes the dominant oscillation mode. This oscillation was identified in ref. [9], but the mechanism responsible for it was unclear.

Subsequent analysis [10] showed this oscillation is thermoacoustic in nature and originates in the exhaust section of the combustor. Phase-averaging showed that this oscillation induces strong radial fluctuations near the combustor walls that are accompanied by a gradual increase in OH* chemiluminescence in the ORZ, indicating that the stable-to-excited state transition results from the coupling of a 635-Hz resonance in the exhaust of the combustor and the outer shear-layer of the reactant inflow. That leads to the transport of hot reacting flow into the ORZ, which destabilizes the outer shear-layer. Absent the stabilizing effect of the outer shear-layer, the flame becomes more susceptible to forcing by the (720-Hz) resonant acoustic mode of the combustor / pressure-vessel and immediately transitions into the excited state.

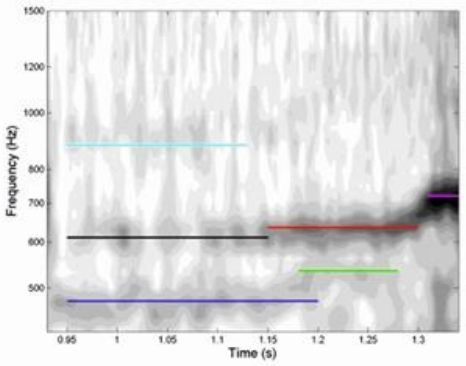

Figure 1.2.8. Morlet-amplitude (envelope) scalogram for axial velocity in the flame region.

Measurement Series B

The goal of Measurement Series B, or "MS-B" was to expand upon the findings of MS-A through the development and application of highspeed tracer-LIF for use in characterizing fuel-air mixing in swirl flames at elevated pressure conditions. Although tracer-LIF (even at kHz acquisition rates) is a well-developed diagnostic technique, its application in swirling flames at elevated pressure and under sooting conditions poses unique and difficult to predict challenges. Nonetheless, these challenges were met and successfully overcome and MS-B may be considered a major success for the project.

AFRL/RDLT Research Engineer Dr. Carrie Noren, supported through the US Air Force "Engineers and Scientists Exchange Program" (ESEP), contributed to the setup and operation of the experimental system deployed in MS-B. The knowledge and experience she gained during this series of measurements may also be considered a positive outcome for both the US Air Force and this project.

Burner

The burner and optically accessible combustion test-rig used in MS-B are the same as those used in MS-A, described in the previous section.

High-Bandwidth Laser Imaging System

The measurement apparatus used in this study is very similar to that deployed in Measurement Series MS-A, albeit updated with new cameras and a significantly more power dye laser for OH-PLIF excitation. The modifications to each system are described (separately) below.

Stereo-PIV System

The stereoscopic-PIV system used the same laser deployed in MS-A (Edgewave, IS200-2-LD), and was operated at 10 kHz. In this measurement series a pair of high framerate CMOS cameras (Phantom V1212, with 1280 by 800 pixels) was deployed. The cameras were each equipped with 72 GB of onboard memory, sufficient for approximately 4 seconds of recording time at full resolution and 10-kHz acquisition rate. The PIV cameras were equipped with 200-mm focal-length, f/4 marco objective lenses (Nikon AF-Micro Nikkor) and a 532-nm-bandpass interference filter to suppress background flame luminosity. The PIV measurement domain covered almost the entire width of the combustion chamber and thus allows for a comprehensive analysis of coherent flow structures (-27 mm < x < 27 mm, 5 mm < y < 27 mm). Inter-frame pulse separation (Δt) was set to 10 μs. The images acquired with this system were processed in a similar manner to those acquired in MS-A. Final interrogation window size and overlap were 24 × 24 pixels and 50%, respectively, for a spatial resolution of 1.9 mm and vector spacing of 0.95 mm. The uncertainty of instantaneous velocities based on the correlation statistics in DaVis was estimated to be ≈ 0.7 m/s for the in-plane components (x-y) and ≈ 1.5 m/s for the out-of-plane component (z axis).

OH-/Acetone-Tracer PLIF System

The OH-/Acetone-PLIF system consists of a *i*) frequency-doubled, Q-switched, diode-pumped solid state Nd:YAG laser (Edgewave IS400-2-L, delivering up to 150 W at 532 nm, though output was limited to ~135 W), *ii*) a frequency-doubled dye laser (pumped by the YAG laser), and *iii*) a pair of *intensified* CMOS camera systems. The dye laser system (Sirah Credo, upgraded with funds supplied through this project) produced 5.3 – 5.5 W (on average, giving 0.53 – 0.55mJ/pulse), at the frequency-doubled wavelength of 283 nm and a pulse-repetition frequency of 10 kHz.

The 283-nm PLIF excitation beam was formed into a sheet approximately 40 mm (high) × 0.2 mm (thick) using three fused-silica, cylindrical lenses (all anti-reflective coated to maximize transmission). The PLIF and PIV laser sheets are overlapped by passing the PIV sheet through the final OH-PLIF turning mirror.

The same laser was used to excite fluorescence signal in both the OH- and the acetone-PLIF imaging systems. For acetone-PLIF, fluorescence signal was imaged via a CMOS camera (LaVision HSS8), an external two-stage intensifier (LaVision HS-IRO), equipped with 85 mm focal length, f/1.2 (Canon) objective and a band pass interference filter. The filter (LOT, 450FS40-50) was centered at 450 nm for detection of the acetone fluorescence and had a bandpass of ±20nm. The OH/acetone-PLIF

measurement domain provides a somewhat larger field of view in comparison with PIV (-27 mm< x < 27 mm, 0 mm< y < 30 mm).

Flames Studied

Two sets of flames were studied in MS-B. The first of these was measured at a pressure of 3 bar with ethylene and air, both injected at ambient temperature. The thermal power and equivalence ratio with respect to the main injector are P=30 kW and φ=1.2, respectively. In addition, secondary air is injected through the ducts at y=80 mm, which results in global values of P and φ of 36 kW and 0.86, respectively. This flame was designed to approximate the reference test case condition known as "International Sooting Flames Workshop – Target Flame 4".

The second set of flames measured in MS-B was designed to replicate the flame conditions studied in MS-A, i.e. at 5 bars pressure, equivalence ratio 0.67 and thermal power of 33kw. One should keep in mind, of course, that for both flame conditions the addition of acetone vapor to the fuel stream will affect the flame chemistry and its propensity to soot. Nonetheless, the relatively low concentration of acetone in the fuel stream is expected to have little effect on the dynamics of fuel-air mixing near the nozzle exit, which are the focus of this series of measurements.

Results and Discussion

As the measurements acquired in MS-B are currently under review for a peer-reviewed journal, an abbreviated discussion of the main findings is provided below.

Mean Acetone-Tracer Distribution

Figure 1.2.9 shows the mean and fluctuating acetone-PLIF signal distributions for both the reacting- and non-reacting, 3 bar, sooting flame condition.

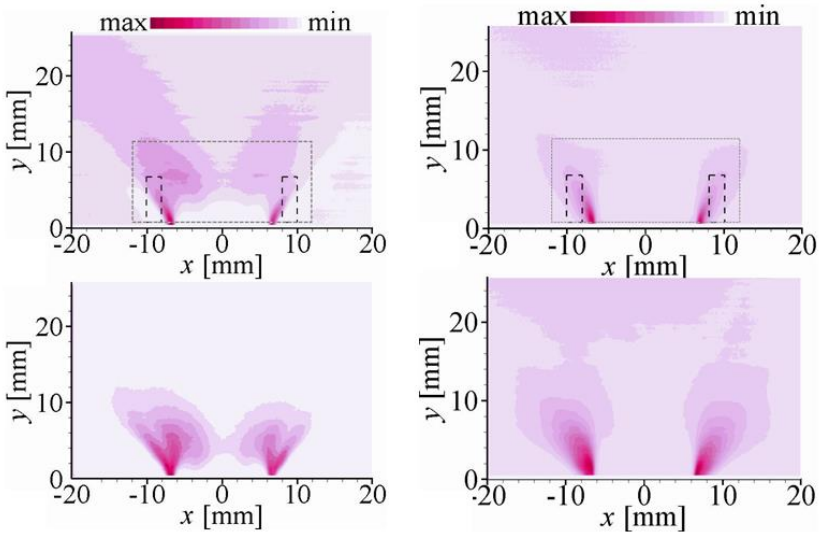

Figure 1.2.9 – Mean (upper) and fluctuating (lower) acetone-PLIF measurements for the non-reacting (left) and reacting (right) flow condition.

Comparison of the reacting- and non-reacting flows suggests the two have similar fuel-air mixing characteristics. The mean fuel concentration is highest in two streaks at the bottom entering from the exit of the fuel injectors underneath. The fuel mixes with air and the mixed fluid is then transported to the IRZ. Mixing appears largely complete within 10mm of the injection point for both cases. Note, the colorbars for the reacting- and non-reacting flows are not identical. In the non-reacting flow, the lack of fuel consumption by a flame results in significant, non-zero fuel concentrations throughout the measurement domain. In the reacting flow, the mean acetone-PLIF signal level drops to almost zero after the main flame zone, resulting in the homogenous background observable in the mean field for that case.

The fluctuating PLIF fields, however, reveal a significant difference in the fuel-air mixing under reacting and non-reacting flow conditions. The fluctuating PLIF signal in the non-reacting flow case shows two distinct branches an each side of the injector centerline. The corresponding mean field shows only a single branch on either side of the centerline. Initial analysis suggests this dual-branch structure is most likely related to the PVC (known to exist in this flowfield, and observed in the PIV measurements) causing lateral displacement and roll-up of the fuel. When the PVC appears in the plane of the laser sheet and interacts with the fuel jet it bends the jet towards the burner centerline. When the PVC passes out of the laser sheet, the jet returns to its initial trajectory along the (mean) shear layer. This periodic lateral forcing results in the dual-peak structure in the fluctuating PLIF

field. The lack of such a structure for the reacting flow case suggests the effect of the PVC on fuel-air mixing is less strong when a flame is present.

For a more detailed understanding of the fuel-air mixing process in the isothermal case, a POD analysis of the acetone-PLIF distributions was carried out for the region of interest (shown as black-dashed rectangle in Fig. 1.2.9).

Figure 1.2.10 shows the energy distribution of the POD modes and the power spectra of the first three temporal POD coefficients. The energy distribution of the acetone-PLIF POD modes can be interpreted as the relative frequency of a specific pattern of fuel distribution in the PLIF measurement series. The spectra of the POD temporal coefficients exhibit a dominant peak at 384 Hz, which (based on analysis of the PIV data) corresponds to the frequency of the PVC in this case. This suggests the fuel distribution is strongly affected by the dynamics of the PVC for the isothermal case.

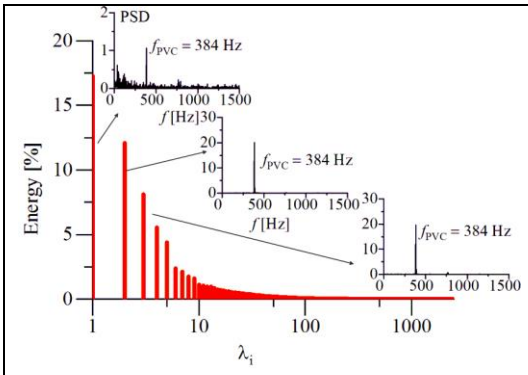

Figure 1.2.10 – POD analysis of non-reacting acetone-PLIF distributions: energy distribution of the POD modes and power spectra of temporal POD coefficients.

Figure 1.2.11 shows acetone-PLIF measurements phase-averaged with respect to the 384Hz precession frequency of the PVC. It is clear from this image sequence that for non-reacting conditions, the PVC has a major impact on the dynamics of fuel-air mixing near the exit of the dual-swirl combustor. Specifically, as the PVC precesses through the field of view of the PLIF imaging system, we see the fuel jet deflect, roll-up, propagate downstream and rapidly dissipate over the course of one precession of the PVC. In the immediate vicinity of the nozzle, this effect appears almost as if the fuel jet were flapping from side to side as the PVC passes it by.

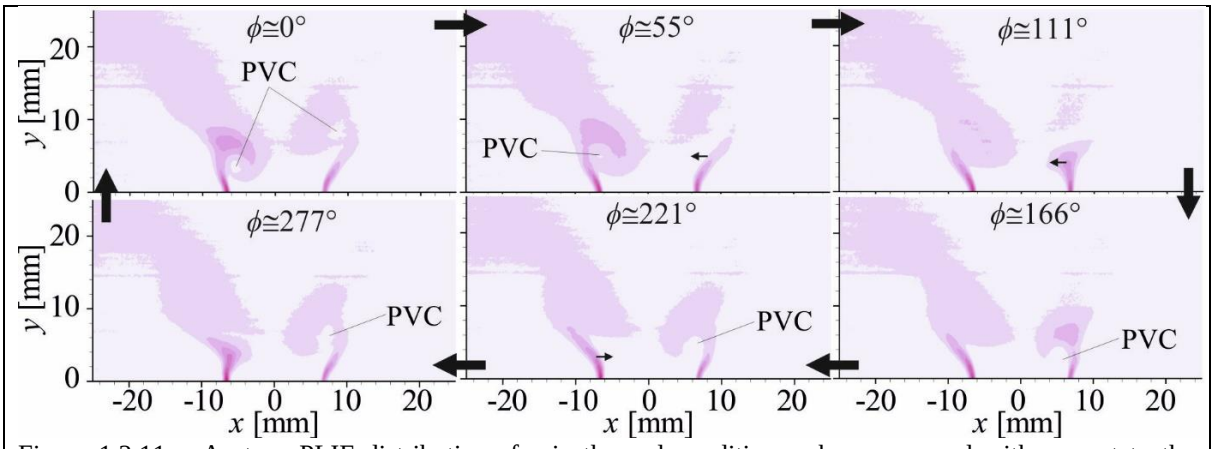

Figure 1.2.11 – Acetone-PLIF distributions for isothermal conditions, phase averaged with respect to the 384 Hz frequency of the dominant flow structure, a precessing vortex core.

A similar POD analysis was applied to the acetone-PLIF distribution for the reacting flow measurement. Figure 1.2.12 shows the energy distribution and power spectra of the temporal POD coefficients. Consistent with the results for the isothermal flow, the majority of signal energy is found in the first three modes. The frequencies of these modes differ significantly though, from those of the isothermal case. In the spectra of the first and second modes, a peak at the frequency of 874 Hz is prominent. Analysis of the PIV data revealed this to be the frequency at which toroidal vortices are shed at the exit of the burner under reacting flow condition studied here. An additional peak is observable in spectra of the temporal coefficient of the third mode at 453 Hz. This was found to represent the influence of a (much weaker) PVC on fuel-air mixing near the exit. Thus, fuel mixing effects in the reacting case are affected by both the toroidal vortex shedding and PVC dynamics at frequencies of 874 Hz and 453 Hz, respectively.

Figure 1.2.13 shows the acetone-PLIF measurements for the reacting flow condition phase-averaged with respect to the a) 874 Hz frequency of the symmetric, toroidal vortex shedding and b) 453 Hz frequency of the PVC structures. The effect of each periodic flow-structure on the fuel-air mixing is immediately apparent. The toroidal vortex shedding is accompanied by a strong axial pulsation in the fuel stream. This pulsation results in a strong variation in the fuel concentration near the nozzle. As the toroidal vortex propagates downstream from the nozzle, it appears to bend the fuel stream away from the burner centerline, suggesting strong vortex-induced mixing prior to fuel burn-out.

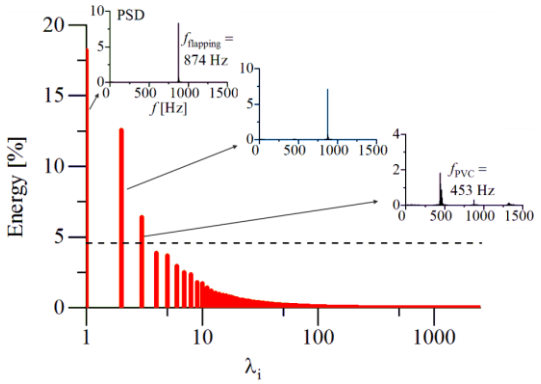

Figure 1.2.12 – POD analysis of reacting flow acetone-PLIF distributions: energy distribution of the POD modes and power spectra of temporal POD coefficients based on the acetone-PLIF data.

The effect of the PVC on fuel-air mixing is much less pronounced for the reacting flow condition than for isothermal flow, but is significant nonetheless. As can be seen in Figure 1.2.13b, the 453 Hz PVC is accompanied by a periodic left-right fluctuation of the fuel near the nozzle, and a slight bending of the fuel jet inward to the burner centerline.

It is noteworthy that the heat release of the flame does not appear strongly affected by oscillations in fuel distribution associated with either vortex structure. The flame does not exhibit strong, self-excited thermoacoustic pulsation at this condition. This may be due to the fact that the condition is rich (with an equivalence ratio of 1.2 in the primary flame zone), and combustion is augmented by downstream air injection.

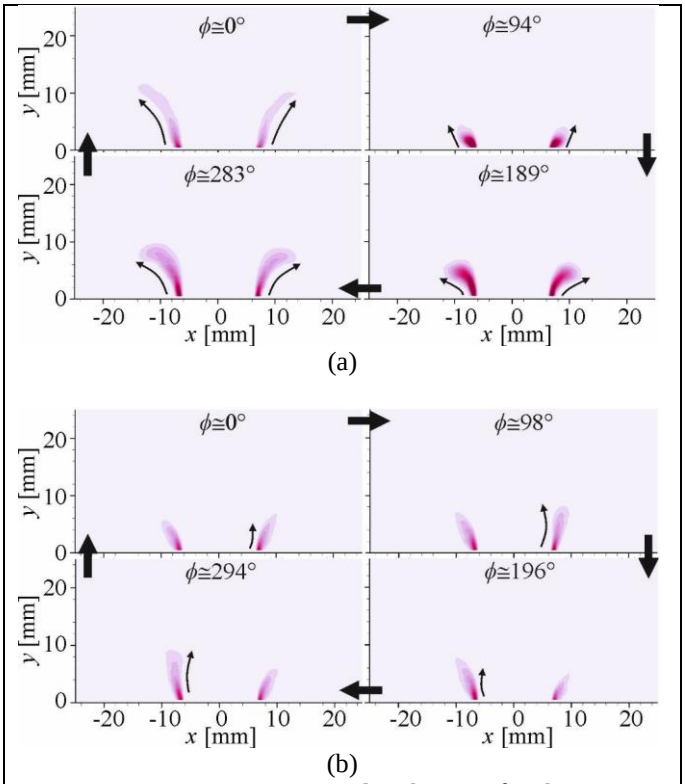

Figure 1.2.13 – Acetone-PLIF distributions for the reacting flow test condition, phase averaged with respect to the a) 874 Hz frequency of the symmetric, toroidal vortex shedding and b) 453 Hz frequency of the PVC structures.

The measurements acquired in MS-B show that the PVC and toroidal vortex shedding at the nozzle cause a regular sequence of flame roll-up, mixing of burned and unburned gases, and subsequent ignition of the mixture in both the inner and the outer shear layers of the dual-swirl burner. This result indicates that the mixing time can be extremely short ($\Delta t = 0.2$ ms).

Although the discussion above focuses on the sooting flame condition measured at 3 bars pressure, analysis of the measurements acquired in lean flames during MS-B is also ongoing. This is analysis is being undertaken in collaboration with fellow AFOSR-sponsored collaborator Professor Jacqueline O'Connor at the Pennsylvania State University, in State College, PA. Due to prolonged discussions between the legal teams of our two research groups over matters related to intellectual property rights, export control law, etc, this collaboration got off to a late start and therefore results of this effort are not yet ready for publication in this report. It is expected however that this collaboration will yield significant new insight into dynamic mixing processes and flow-flame interaction in lean, swirl-stabilized flames in the dual-swirl combustor.

Measurement Series C

The benchtop-scale high pressure combustion test facility used in Measurement Series A and B limited the range of combustor pressures we were able to achieve to approximately 7 bars. To address this limitation, a new version of the dual-swirl burner was developed for use in the DLR-HIPOT, an optically-accessible test rig capable of operation at up to 35 bars pressure and 300kW thermal load. The availability of this new burner enabled us to reach significantly higher combustor pressures and thereby achieve a key project goal during an experimental campaign performed at the German Aerospace Center in the summer of 2017. This campaign was completed together with AFRL Engineer (and long-time DLR collaborator) Dr. Campbell Carter. Dr. Carter's visit was supported through the AFOSR "Windows on the World" program.

Burner

The burner used in measurement series MS-C is of the same basic design as the one used in MS-A and MS-B, albeit modified for installation in the DLR-HIPOT facility. The burner consists of a swirled fuel-air injector coupled to an optically accessible combustion chamber. The geometry and dimensions of swirl injector match those of the burner used in MS-A. In contrast with the measurements of MS-A (which used ethylene), the fuel used in this experiment was natural gas. In addition, the exit planes of both the fuel and the air flows are located at the level of the combustion chamber inlet, ensuring maximal optical access to flame dynamics at the nozzle exit.

The combustion chamber has a square cross-section measuring 85 × 85 mm^2 and is 200mm long. It has four fused silica windows and a water-cooled end cap with a contoured exit contraction. This chamber is mounted in a water-cooled stainless steel pressure vessel with four large windows for optical access. The chamber pressure is adjusted via an adjustable throttle located downstream of the pressure vessel. The HIPOT test rig is mounted on a 3-axis translation system, to enable re-positioning of the test article during operation without the need to re-align or otherwise adjust the optical diagnostic systems mounted around it.

High-Bandwidth Laser Imaging System

The measurement apparatus used in this study is essentially the same as that deployed in Measurement Series MS-A, albeit updated with new cameras and a significantly more power dye laser for OH-PLIF excitation. The modifications to each system are described (separately) below.

Stereo-PIV System

The stereoscopic-PIV system used the same laser deployed in MS-A (Edgewave, IS200-2-LD), and was operated at 10 kHz. In this measurement series a pair of high framerate CMOS cameras (Phantom V1212, with 1280 by 800 pixels) was deployed. The cameras were each equipped with 72 GB of onboard memory, sufficient for approximately 4 seconds of recording time at full resolution and 10-kHz acquisition rate. The PIV cameras were equipped with 200-mm focal-length, f/4 marco objective lenses (Nikon AF-Micro Nikkor) and a 532-nm-bandpass interference filter to suppress background flame luminosity. The images acquired with this system were processed in a similar manner to those acquired in MS-A. The resulting 3-component velocity field is composed of 50 × 80 = 4000 independent vectors, with ca. 1mm spatial resolution.

OH-PLIF System

The OH-PLIF system consists of a *i*) frequency-doubled, Q-switched, diode-pumped solid state Nd:YAG laser (Edgewave IS400-2-L, delivering ≈135 W at 532nm), *ii*) a frequency-doubled dye laser (pumped by the YAG laser), and *iii*) an *intensified* CMOS camera system. The dye laser system (Sirah Credo) produced 4 – 4.5 W (on average, giving 0.4 – 0.45 mJ/pulse), at the frequency-doubled wavelength of 283 nm and a pulse-repetition frequency of 10 kHz.

The 283-nm PLIF excitation beam was formed into a sheet approximately 40 mm (high) × 0.2 mm (thick) using three fused-silica, cylindrical lenses (all *anti-reflective* coated to maximize transmission), and the OH-PLIF and PIV laser sheets are overlapped by passing the PIV sheet through the final OH-PLIF turning mirror. In contrast with the experimental setup used in MS-A, both PIV and PLIF laser sheets were formed above the HIPOT test rig using optics mounted on X-95 rail and

directed down into the chamber through the top windows. While this was a good, robust configuration, it was also a real challenge to set up, adjust and align (as myriad combustor and optical components were in the way).

Fluorescence from the A–X (0,0) band was acquired with a CMOS camera (LaVision HSS8), an external two-stage intensifier (LaVision HS-IRO), and a Halle 64-mm focal length, f/2 UV lens. Elastic scattering (at 283 nm from the PIV seed particles) was blocked with the use of a high-transmission (> 80% at 310 nm) bandpass filter while background flame emission is further attenuated with a 100-ns intensifier gate.

OH Chemiluminescence Imaging System*

A second intensified camera, placed opposite to the PLIF cameras, (i.e. on the other side of the high-pressure chamber) was employed to record OH chemiluminescence. The camera, a high-speed CMOS imaging system (LaVision HSS8), was equipped with an external, two-stage, lens-coupled intensifier (LaVision HS-IRO) and fitted with a 45 mm focal length, f/1.8 objective (Cerco) and a high-transmission, band-pass interference filter. The integration time for the chemiluminescence signal (equaling the intensifier gate time) was 5 μs.

Flames Studied

The test matrix for MS-C was designed to hold as many flow and flame variables constant as possible as chamber pressure was increased. This included global stoichiometry, reactant temperature and air-split ratio (i.e. the percentage of total air put through the center- vs. the outer swirl nozzle). It would have been preferable to keep bulk flow velocity constant with increasing chamber pressure but this was impossible to achieve without triggering strong, self-excited thermoacoustic pulsation in the combustor. Such pulsation can lead to blow-out of the flame or worse, damage to the test rig. Table 3 summarizes the operating conditions studied in this series of measurements;

Table 3 – Operating Conditions Measure

Pressure (bars)	Equivalence Ratio - ϕ	Total air flow rate (g/s)	Thermal Load (kW)
1	1	13.32	40
5	0.77	66.6	152
10	0.77	100	230
11	0.77	87.9	201
12	0.77	95.9	220
13	0.77	103.9	238
14	0.77	111.9	256
15	0.77	119.9	274

Results and Discussion

The measurement campaign (MS-C) had two primary outcomes. First, it yielded data that enabled us to test the feasibility and limitations of acquiring high-bandwidth laser imaging measurements in turbulent flames at pressures of up to 15 bars with commercially available equipment. Second, it helped develop and expand the technical "know-how" required to successfully implement and optimize this challenging measurement technique.

Figure 1.2.14 shows a sample set of false-color OH-PLIF images from this dataset for combustor pressures ranging from 5 to 15 bars. Here, one can see the strong effect of combustor pressure on signal levels, as the maximum of the color table drops by a factor of 4 when the combustor pressure increases from 5 bars to 15 bars. (Indeed, the decrease in signal is much more dramatic when the dataset from 1 bar is included.) Other practical challenges are also evident in these images; for example, horizontal streaks of some residue showed up between operation at 10 bars and 13 bars, and of course, the lower signal level attendant with high pressure means that image noise is higher and contrast (between reactants/fuel and combustion products) is lower. Nonetheless, these images show the potential for kHz-rate measurements at high combustor pressures. Analysis of these measurements is ongoing at the time of writing of this report.

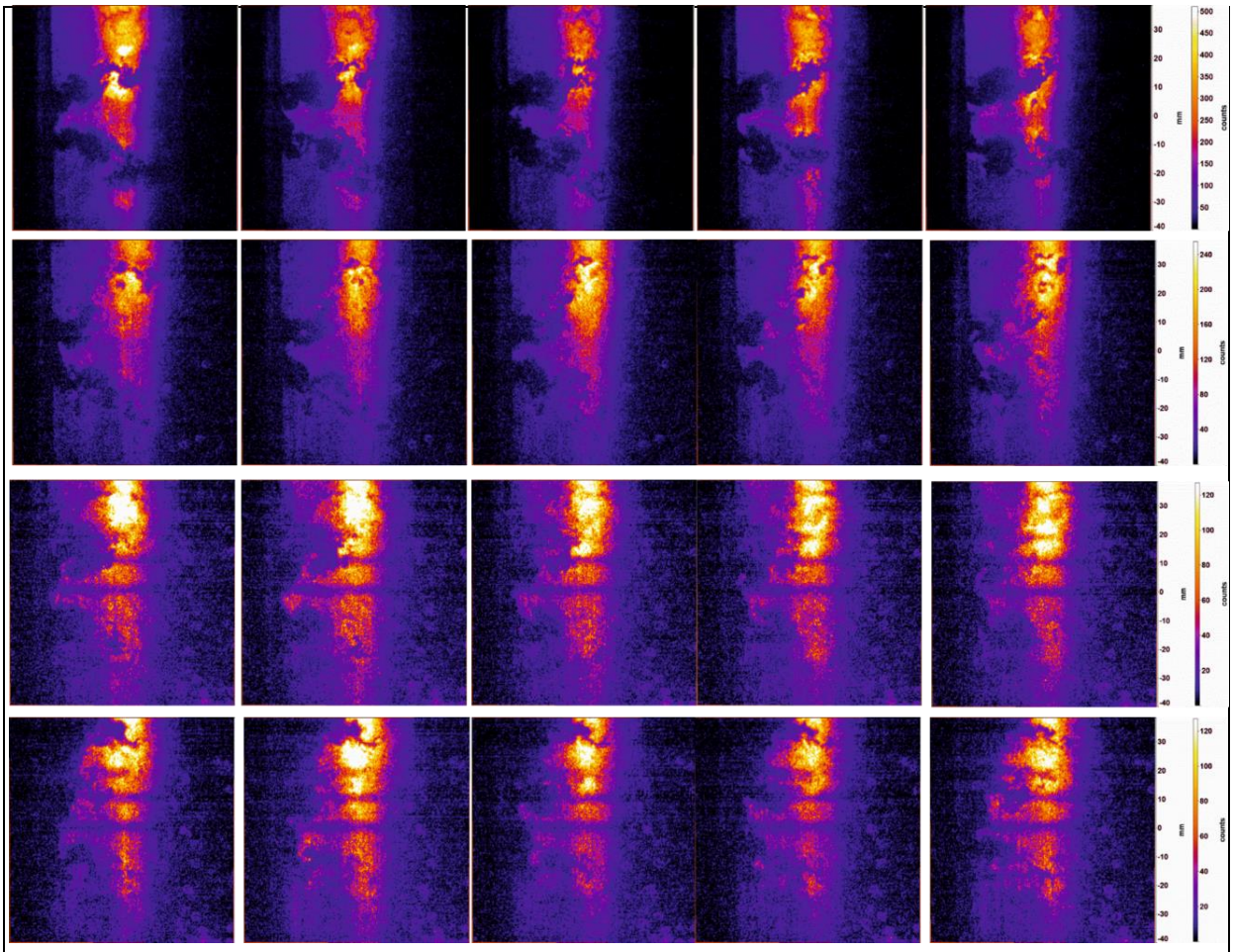

Figure 1.2.14 - Sample OH-PLIF images from the dual swirl burner in the HIPOT. Rows 1-4 show 5 consecutive images (Δt = 0.1 ms) at pressures of 5, 10, 13, and15 bars. Flow is from left to right in each frame, and the laser sheet skimmed the bottom floor of the combustor. The images have been corrected for detector nonuniformity but not for the variation in laser sheet intensity; color scaling is shown with the color bar at the right of each row.

Figure 1.2.15 shows several photographs of the experimental setup used in this study. These photographs are shown to illustrate the some of the practical challenges of performing high bandwidth laser imaging experiments at an industrial scale test rig facility. For example, the available space is limited, which can be challenging when trying to place, adjust and align two lasers, four large cameras, two intensifiers, optics, timing and control equipment. In addition, workplace safety considerations prevent users from adjusting/servicing the equipment during operation and therefore necessitate complete automation and remote control of these finely tuned imaging systems. Indeed, (as the photo in the upper left of Figure 1.2.15 shows), even seemingly simple tasks like taking images of a spatial calibration target become a challenge when one must accurately mount and align that target within a pressure vessel with three planes of thick quartz glass between it and the camera.

These challenges are difficult to predict and even more challenging to address, particularly when under the time pressure associated with having to pay considerable run-time costs for the use of the high-pressure facility. The experience gained and "lessons learned" as a result of the measurement campaign are valuable in the transition of the high bandwidth laser imaging system from use in an optics laboratory to full functionality in a high-pressure combustion test facility.

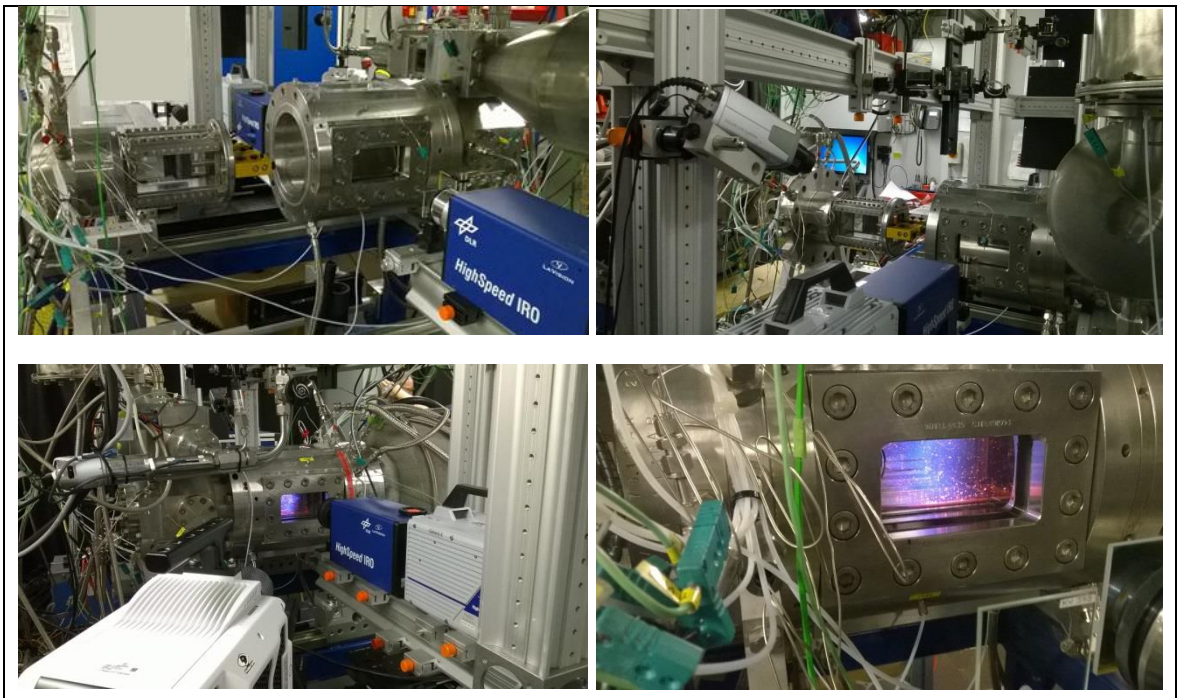

Figure 1.2.15 – Photographs showing the experimental hardware. In the upper row, the HIPOT test rig is open for setup and alignment. In the lower row, the test rig is closed and in operation. Note, the photographs showing the rig in operation were taken immediately after startup, when the rig was still at atmospheric pressure.

Assessment of the Feasibility of High Bandwidth Laser Imaging at Elevated Pressure

Based on the measurements acquired at in both the dual-swirl burner during measurement campaign MS-C, and in the bluff-body stabilized flames during measurement series MS-2, it is now possible to assess the feasibility of high bandwidth laser imaging of turbulent flames at elevated pressure using commercially available DPSS lasers and CMOS imaging systems.

These measurement campaigns revealed OH-PLIF to be the most challenging diagnostic to accomplish at elevated pressure. From the standpoint of practical considerations such as window-fouling and achieving sufficiently dense particle seeding and uniform seed distribution, PIV measurement certainly poses significant challenges, but less so than OH-PLIF. Inspection of the OH-PLIF data, samples of which were shown in Figures 1.1.14 and 1.2.14, indicate good quality imaging data, defined by moderate to high signal levels and with signal-to-noise ratios sufficient to accomplish edge detection is possible in lean, turbulent flames at pressures of up to 10 bars. Although it is impossible to prove a negative, the results also suggest that OH-PLIF imaging in lean flames at pressures beyond 10 bars pressure will likely yield data unsuitable for robust edge-detection (necessary for computation of parameters such as flame surface density and local flame curvature). At pressures between 10 and 15 bars, it appears viable to acquire OH-PLIF images with quality sufficient for qualitative flow visualization purposes.

Section 2 – Multilateral Collaborations with American Universities

This project was motivated by a mutual interest from AFOSR and DLR to transition highspeed laser imaging diagnostics from the optics laboratory to functionality in high pressure combustion test facilities. To realize the full benefit of this shared objective, it was essential that the knowledge and experience gained in this project be shared effectively with the wider combustion research community. Given the complexity of this measurement technique, the most effective way to do this is through close, one-on-one technical collaborations. Therefore, during the course of this project, I (principal investigator Dr. Isaac Boxx) made three visits to the USA to undertake short-term joint research projects with groups based at US Universities. Each visit was approximately three weeks in duration, and involved a research group supported under the Air Force Office of Scientific Research Basic Combustion Research (AFOSR-BCR) program.

The first collaboration was with Professor Jacqueline O'Connor, at the Pennsylvania State University, in April, 2017. The second was with Professor Kareem Ahmed, at the University of Central Florida in April, 2018. The third collaboration was with Professor Venkat Narayanaswamy at the North Carolina State University in April, 2019. Each collaboration is described (separately) below.

Section 2.1 - Joint measurement campaign with Professor Jacqueline O'Connor and Ankit Tyagi of Pennsylvania State University, on flame-flame interaction.

Introduction / Background

In April, 2017, I travelled to State College, Pennsylvania to conduct a joint measurement campaign with Professor Jacqueline O'Connor at the Pennsylvania State University. This campaign was three weeks in duration. The goal of this campaign was twofold. First, it was to exchange knowledge, experience and "know-how" about high bandwidth laser imaging techniques with another AFOSR-supported research team. Second. It was to acquire a series of high bandwidth laser imaging measurements of turbulent flames generated in the Penn State Dual Flame Burner. Both of these goals were successfully achieved and the collaboration was a resounding success.

Experiment

Burner

The Penn State Dual-Flame Burner is shown in Figure 2.1.1. It consists of two identical, premixed slot burners with 100mm × 10mm exit planes. The burners can be operated either as Bunsen- or bluff-body stabilized burners. Each burner consists of a lower and an upper section, which measure 178mm and 160mm tall, respectively. The lower section contains the inlet for the premixed reactants (in this study, natural gas and air), and a ceramic honeycomb flow-straightener. The upper section contains an additional ceramic honeycomb flow straightener and two perforated plate turbulence generators. These plates have 3.175mm hole-diameters, 40% open area and are mounted 30- and 10mm upstream of the burner exit. The perforated plates are designed to produce a uniform flow with homogenous isotropic turbulence at the burner exit and are specified according to the empirical correlations presented is Roach [11]. Each burner also contains two pilots, a thin pilot flame aligned with the 100mm edge of the burner exit to anchor the flame and much wider outer pilot to back-support the flames downstream with hot combustion products.

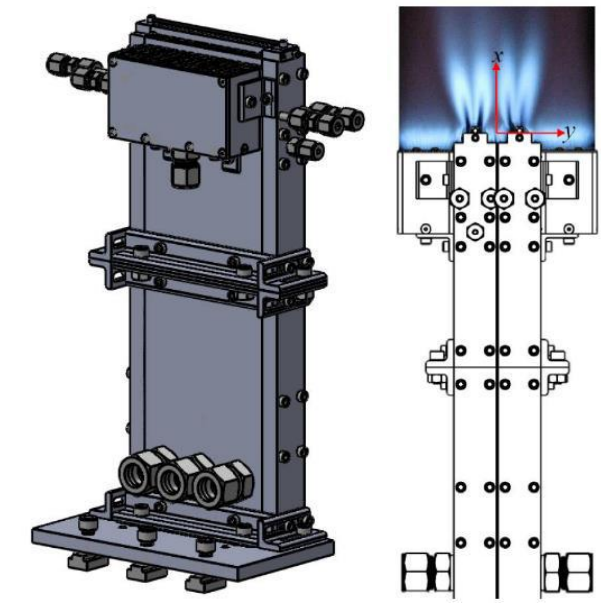

Figure 2.1.1 – Penn State Dual Flame Burner.

Diagnostics

The high bandwidth laser imaging system (shown schematically in Figure 2.1.2) deployed in this study is quite similar to the one I have developed over the past ten years at the German Aerospace Center, in part with support of several EOARD and AFOSR research grants. It consists of a kHz acquisition-rate planar laser-induced fluorescence system combined with a (simultaneously operated) stereoscopic particle image velocimetry system. A brief description of each element is provided below.

Planar Laser-Induced Fluorescence

The OH-PLIF system used a frequency-doubled dye laser (Sirah Credo, using Rhodamine 6G in ethanol), driven by a frequency-doubled, diode-pumped solid state laser (Edgewave IS-811E, 80W time-average power output at 532nm and 10kHz). The laser was operated at 282.9 nm and tuned to the Q1(6) line of the A-X (1,0) band of OH. At 10 kHz it delivered approximately 300 μJ/pulse.

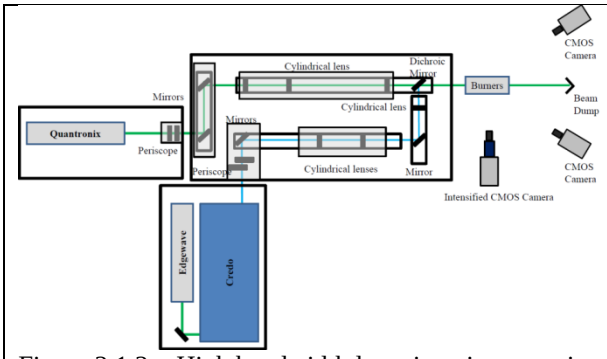

Figure 2.1.2 – High bandwidth laser imaging experiment configuration.

The beam was formed into a sheet of ≈ 21 mm (high in the probe region) using two fused silica lenses (f = -37.5, +750 mm) and focused to a waist using a third cylindrical lens (f = 750 mm) and overlapped with the PIV beam using a pair of dichroic mirrors. Fluorescence signal was acquired with a CMOS camera (Photron FASTCAM SA1.1), external two-stage, lens-coupled intensifier (LaVision HS-IRO, 100ns integration time), a 100 mm, f/2.8 objective (Cerco) and bandpass interference filter. This lens was one item among several that were generously loaned to Professor O'Connor by AFRL researcher Dr. Campbell Carter.

Stereo-PIV System

The SPIV system consisted of a dual-cavity, diode-pumped, solid state laser (Quantronix Hawk Duo, up to 9mJ/pulse at 532nm) and a pair of CMOS cameras (Photron FASTCAM SA5) mounted on opposite sides of the laser sheet in a forward-scatter configuration. The camera were equipped with 100mm, f/2.8 macro lenses (Tokina). The intense thermal radiation of the flames necessitated placement of the cameras considerably further away from the burners than might otherwise be desirable, affecting the magnification and field of view of the cameras. To compensate for this, (2x magnification) teleconverters were installed between the macro lenses and each camera. Scheimpflug-adaptors were used to compensate for defocussing of the images caused by off-axis imaging. Image distortion due to off-axis orientation of the cameras was corrected using a dual-plane image target (LaVision, Type 106-10). The same target was also used for mapping the fields of view of the SPIV and PLIF systems to one another.

PIV image pairs were acquired at 10 kHz and 704 × 520 pixel resolution. Interframe pulse separation (Δt) was 14 μs. The beam was formed into a sheet using a pair of cylindrical lenses (f= -35, +250 mm) and thinned to a waist using a third cylindrical lens (f = 700 mm). The flow was seeded with aluminum oxide (AlO_2) particles of diameter 0.5–2 μm. Image mapping, calibration, and particle cross-correlations were completed using a commercial, multi-pass adaptive window offset cross-correlation algorithm (LaVision DaVis 8.3). Final interrogation window size and overlap were 16 × 16 pixels and 50%, respectively, for a spatial resolution of 0.96 mm and vector spacing of 0.48 mm. Based on the ± 0.1 pixel uncertainty of the cross-correlation peak-finding algorithm, the random uncertainty of the PIV measurements is estimated to be ± 0.43 m/s.

Flow Configuration(s)

The Penn State Dual-Flame Burner is a highly versatile facility, which gives users control over parameters including burner separation, pilot and back support configurations, flame configuration (Bunsen vs bluff-body stabilized) and mean shear across the reaction zone. Although the majority of measurements were taken after my departure, Table 4 provides a summary of the test conditions measured by PhD candidate Ankit Tyagi.

OH-PLIF cases

Flame configuration	Pilot flames	U [m/s]	Re	Re_D	ϕ	u' [m/s]	l [mm]	u'/s_L	l/l_f	Re_l	S [mm]
Bunsen	All	12	15484	--	1	2.63	1.82	6.57	2.6	340	30
Bunsen	Anchoring	20	25808	--	1	4.32	1.83	10.8	2.62	561	30
Bunsen	Anchoring	24	30969	--	1	5.36	1.88	13.4	2.69	715	30
Bluff-body	All	12	15484	2704	1	2.63	1.82	6.57	2.6	340	30
Bluff-body	--	12	15484	2704	1	2.63	1.82	6.57	2.6	340	35
Bluff-body	--	12	15484	2704	1	2.63	1.82	6.57	2.6	340	40

CH* chemiluminescence cases

Flame configuration	Pilot flames	U [m/s]	Re	Re_D	ϕ	u' [m/s]	l [mm]	u'/s_L	l/l_f	Re_l	S [mm]
Bunsen	Back-support	15	19356	--	1	3.33	2.22	8.28	3.18	525	40
Bunsen	Back-support	15	19356	--	1	3.33	2.22	8.28	3.18	525	40
Bluff-body	Back-support	15	19356	3380	1	3.33	2.22	8.28	3.18	525	52
Bluff-body	Back-support	15	19356	3380	1	3.33	2.22	8.28	3.18	525	52
Bunsen	Back-support	18	23227	--	1	4	2.19	9.94	3.14	622	40
Bunsen	Back-support	18	23227	--	1	4	2.19	9.94	3.14	622	40
Bluff-body	Back-support	18	23227	4056	1	4	2.19	9.94	3.14	622	52
Bluff-body	Back-support	18	23227	4056	1	4	2.19	9.94	3.14	622	52

Table 4 – Test conditions measured in the Penn State Dual-Flame Burner by Ankit Tyagi and co-workers.

Results and Discussion

High bandwidth laser imaging is a sophisticated diagnostic technique that requires careful training and years of experience to successfully master. A key goal of this collaborative research project is to share knowledge, experience and best practices acquired over the past decade at the German Aerospace Center with US-based research groups during exchange visits such as this one.

Figure 2.1.3 shows a number of photographs of the experimental setup described above. It is shown here to illustrate the complexity of this experiment. Prior to my arrival at Professor O'Connor's laboratory, we had undertaken several planning and coordination meetings and upon my arrival much of the equipment required for the experiment was available. Nonetheless, the majority of the three week visit was spent building up, aligning and calibrating the measurement system. Such setup and alignment work can be exhausting, both mentally and physically but the hard work and enthusiasm of the Penn State research team made is a rather enjoyable and fulfilling experience. By the end of my visit, the experiment had been fully built, aligned, calibrated and the first data acquired. In addition, and perhaps more importantly, the Penn State research team was well-trained and sufficiently experienced in high bandwidth laser diagnostics to successfully operate the system upon my departure. It is therefore quite fair to declare this research visit a resounding success.

Although the key goal of this research collaboration was to share knowledge and experience in high bandwidth laser imaging techniques, the measurements it enabled have yielded considerable scientific insight into flame-flame and flow-flame interaction and the role of mean shear on turbulent flame dynamics. The measurements and related analysis have been published in three peer-reviewed journal papers and several scientific and technical meetings. The reader is referred to these publications for a more detailed description of the scientific findings;

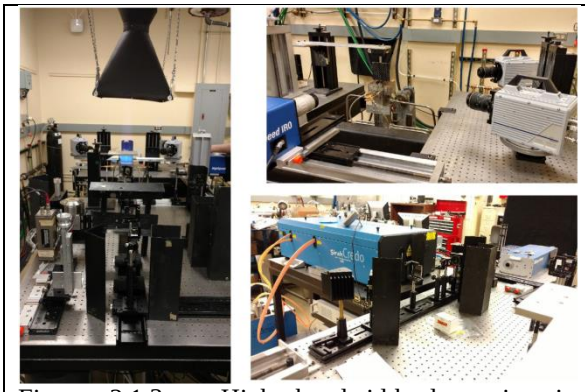

Figure 2.1.3 – High bandwidth laser imaging experiment at Professor O'Connor's laboratory at the Pennsylvania State University.

Journal Publications

1. Tyagi, A., Boxx, I., Peluso, S., O'Connor, J. (2020) "Pocket formation and behavior in turbulent premixed flames". Combust. Flame 211, pp. 312-324.
2. A. Tyagi, I. Boxx, S. Peluso, J.O'Connor. (2019). "Statistics and Topology of Local Flame-Flame Interactions in Turbulent Flames", Combust. Flame 203 (2019), 92-104
3. A. Tyagi, I. Boxx, S. Peluso, J.O'Connor (2018). "The role of flow interaction in flame-flame interaction events in a dual burner experiment", Proc. Combust. Inst. 37:2 (2018). 2485-2491.

Conference Papers

1. A. Tyagi, I.G. Boxx, S. Peluso, J. O'Connor. "Statistics of Local Flame-Flame Interactions in Flame Interaction Zones of Two V-Flames", AIAA-2019-0446. AIAA SciTech 2019 Forum. San Diego, California.
2. A. Tyagi, I.G. Boxx, S. Peluso, R. Shupp, J. O'Connor. "Structure of flames in flame interaction zones", AIAA 2018-0161. 2018 AIAA Aerospace Sciences Meeting, 8 – 12 January, 2018. Kissimmee, Florida.

Section 2.2 - Joint measurement campaign with Professor Kareem Ahmed of the University of Central Florida, on premixed, turbulent bluff-body stabilized flames

Introduction / Background

In April, 2018, I travelled to Orlando, Florida to conduct a joint measurement campaign with Professor Kareem Ahmed at the University of Central Florida. This campaign was three weeks in duration. The goal of this campaign was twofold. First, it was to exchange knowledge, experience and "know-how" about high bandwidth laser imaging techniques with another AFOSR-supported research team. Second. It was to acquire a series of high bandwidth laser imaging measurements of premixed, turbulent bluff-body stabilized flames in straight-, converging- and diverging ducts. Both of these goals were successfully achieve and the collaboration was a success.

Experiment

The goal of this study was to understand the role of near-field, flame-generated vorticity on the stability and blow-out characteristics of turbulent, premixed bluff-body stabilized flames. This was accomplished by acquiring long-duration high-speed measurements of the flow-field and chemiluminescence emissions of a series of bluff-body stabilized flames in a rectangular cross-section combustion wind tunnel with straight-, converging- and diverging flame confinement sections. The combustion facility and optical diagnostics system are described (separately) below.

Combustion Facility

Experiments were conducted in the high-speed blow-down wind-tunnel facility shown in Figure 2.2.1. In this facility, a premixed propane-air mixture from a 50mm pipe is delivered to the facility through a conical-to-rectangular diffuser with an exit area of 155 × 130 mm. From there the flow passes through a series of four wire-mesh flow-conditioning screens. These use grids of 1 mm diameter wire to form screens with 4 mm characteristic length and 64% open area. After passing these screens, the flow enters the (45 × 127 mm) combustor through a nozzle. The 3.5:1 area ratio, fifth-order polynomial profile nozzle contraction is designed to ensure a uniform velocity profile at the entrance of the combustion section.

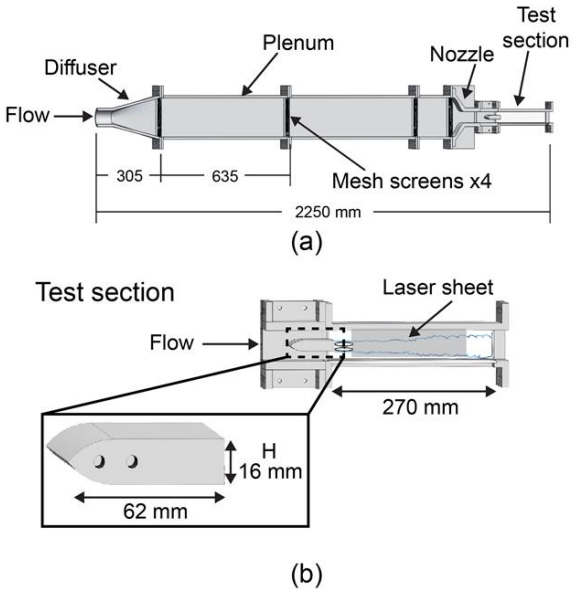

Figure 2.2.1 – a) UCF High speed blow-down wind-tunnel facility, b) Bluff-body stabilized burner

Flames in this combustor are stabilized using the ballistic-type bluff-body shown in Figure 2.2.1. The height and length of the bluff-body are 16 and 64 mm, respectively. It is positioned on the axial centerline of the combustor and spans the full width of the test section.

Downstream of the bluff body is an optically accessible confinement section with cross-sectional dimensions of 45 × 127 mm. The top and bottom walls of the confinement section are adjustable, enabling it to act either as a straight rectangular duct, a diffuser, or a nozzle. In the diffuser and nozzle configurations the top and bottom walls are set at positive and negative 3-degree angles, respectively. The lower- and side walls of this section are made of quartz glass plates to allow optical access for laser diagnostic measurements. The upper wall is made of stainless steel and is equipped a series of pressure taps every 3.18 mm along its length. These taps are connected to a pressure transducer to measure static pressure along the wall for each configuration. The upper wall is painted black to minimize back-reflection of the laser sheet during measurements.

Flow Conditions

The fuel (propane) flow was controlled with a rotameter, pressure regulator, and a shut-off valve to achieve an equivalence ratio of $\phi = 0.7$. The free-stream velocity at the test-section (at the trailing edge of the bluff-body) of the propane-air mixture was maintained at 25 m/s.

Optical Diagnostics

Three highspeed imaging systems were employed simultaneously in this study; 1) a wide-field, two-component particle image velocimetry system, 2) a narrow-field, high spatial resolution stereoscopic PIV (SPIV) system, and 3) a C2*/CH* chemiluminescence imaging system. The utility of having two overlapping PIV systems is that it enables us to place the high-resolution, narrow field SPIV measurements into the context of the overall flow-field. Each system is described (separately) below.

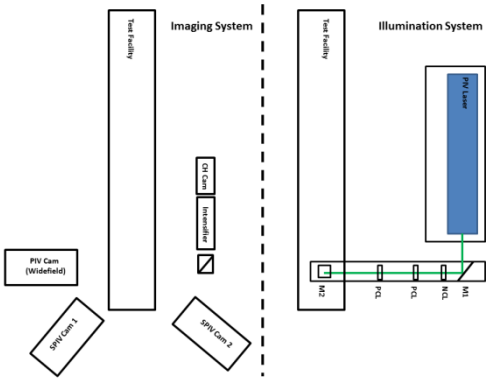

Figure 2.2.2 – Optical Diagnostics System. Left – Imaging Systems, Right – Laser illumination system.

Wide-Field PIV

The wide-field PIV system consists of a highspeed laser, sheet-forming optics and a camera mounted perpendicularly to the flow facility as shown in Figure 2.2.2.

A dual-cavity, diode pumped solid state (Nd:YAG) laser was used to illuminate aluminum oxide particles seeded into the flow. The particles had a nominal diameter of 150nm and were introduced to the flow well upstream of the flow facility from a separately metered particle seeder. The laser has a wavelength of 532nm and generates pairs of (12mJ) pulses at 10kHz repetition rate. In this study the time separation for each pulse-pair was set to 50μs, which effectively doubles the acquisition-rate of the PIV system from 10 kHz to 20 kHz, albeit with some reduction in dynamic range. The beam was formed into a sheet of approximately 70 mm in height using a pair of cylindrical lenses (focal lengths -25 mm and +450 mm) and focused to a thin waste at the test section using a 1000 mm focal length cylindrical lens. The beam was introduced to the test section via a turning mirror mounted below the flow facility.

Elastic scattering from the alumina particles was imaged using a highspeed CMOS camera (Photron SA-5) mounted perpendicular to the flow facility, as shown in Figure 2.2.2. The camera has a 1024 × 1024 pixel imaging array and was equipped with a 50mm focal length, f/1.2 imaging objective (Nikon Nikkor). At 20kHz acquisition rate the CMOS array was operated in partial frame readout mode, with dimensions 512 × 512 pixels. This imaging configuration resulted in a pixel resolution of approximately 0.125 mm/pixel and overall field of view of 64 × 64 mm.

Velocity vectors were determined via cross-correlation of sequential images. This was accomplished using a commercially available software package (LaVision Davis 8.0) with a multi-pass adaptive window offset cross-correlation function. The final interrogation window size and overlap were 16 × 16 pixels and 50% respectively for a spatial resolution of 2 mm/vector and vector spacing of 1 mm.

High Resolution Stereo-PIV

The SPIV system consisted of a highspeed laser and a pair of highspeed cameras mounted on opposite sides of the flow facility, as shown in Figure 2.2.2. The SPIV system used the same laser and sheet-forming optics as that of the wide-field PIV system described above. The field of view of the SPIV cameras was nested within that of the wide-field system and images were acquired using both systems simultaneously.

Elastic scattering from the alumina particles was imaged with a pair of highspeed CMOS cameras (Photron SA-Z) mounted symmetrically on either side of the flow facility, as shown in Figure 2.2.2. Each camera was equipped with a 180mm focal length, f/4 macro objective lens (Tamron). The relatively low luminosity of the flames in this study, together with the short exposure time of the cameras rendered the use of bandpass interference filters in front of the cameras unnecessary. Camera-mounted scheimpflug adaptors were used to mitigate the image blur attendant with off-axis imaging in

a stereoscopic configuration. This imaging configuration resulted in a field of view of 25 × 25mm, with image size of 1024 × 1024 pixels.

Measurement acquisition time in this study was limited by the size of the onboard memory in the highspeed camera systems. The SPIV cameras are equipped with sufficient memory to acquire 5454 full-frame images, or 0.273s acquisition at the 20kHz (effective) SPIV acquisition rate. Velocity vectors were determined via cross-correlation of sequential images using the same software package (LaVision Davis 8.0) as for the wide-field PIV system. The final interrogation window size and overlap were 16 × 16 pixels and 50% respectively, for a spatial resolution of 0.4mm/vector and vector spacing of 0.2 mm.

C2/CH* Chemiluminescence Imaging*

The C2*/CH* chemiluminescence imaging system used in this study is described in detail in [12]. It consists an imaging objective, an image splitter, two band-pass filters and a highspeed CMOS camera mounted beside the flow facility as shown in Figure 2.2.2.

Self-excited chemiluminescence from the C2* and CH* flame radicals was collected through a 50mm, f/1.2 objective lens (Nikon Nikkor) mounted to an image splitter. Narrow-band wavelength filters are used to isolate the 422-432 nm band of CH*- and 505-522nm band of C2*-chemiluminescence. These two filtered signals are imaged onto a CMOS camera (Photron SA5) equipped with an external, lens-coupled intensifier. This imaging configuration resulted in a field of view measuring 64 × 45 mm.

Results and Discussion

Figure 2.2.3 shows a photograph of the experimental setup described above. It is shown here to illustrate the complexity of this challenging experiment. Prior to my arrival at Professor Ahmed's laboratory, we had undertaken several planning and coordination meetings, both on site and via telephone. Upon my arrival, some of the equipment required for the experiment was already available. Various components which were not available at the laboratory were generously loaned to us by Dr. Campbell Carter of the Air Force Research Laboratory and by LaVision Inc. This included optics, camera objective lenses and scheimpflug adaptors. Various other components were borrowed from other UCF laboratories or fabricated by the lead student collaborator Jonathan Reyes during the course of the measurement campaign.

The majority of the three week visit was spent building up, aligning and calibrating the measurement system. By the end of my visit, the experiment and diagnostic systems were fully operational. In addition, and perhaps more importantly, the UCF research team was well-trained and sufficiently experienced in high bandwidth laser diagnostics to successfully operate the system upon my departure, which they did. It is therefore reasonable to declare this research visit a success.

Figure 2.2.3 – High bandwidth laser imaging experiment at Professor Ahmed's laboratory at the University of Central Florida.

Although the key goal of this research collaboration was to share knowledge and experience in high bandwidth laser imaging techniques, the measurements it has enabled have yielded considerable new insight into the influence of flame-generated vorticity on lean flame extinction. Figure 2.2.4, for example, shows the instantaneous (measured) flame location superimposed onto the vorticity field contour for each flow channel configuration for times approaching blow-out. The flame-edge is color coded according to the measured strain-rate along it. The flame edge is generally observed to reside outside the region of high vorticity in the bluff-body wake. As the flame proceeds to extinction, parts of the flame-edge begin to overlap with the regions of high vorticity close to the bluff-body and the general flame symmetry is lost. High strain-rates are observed in regions where there is an overlap between the flame edge and pockets of high vorticity, suggesting that this is a triggering event for eventual blow-out.

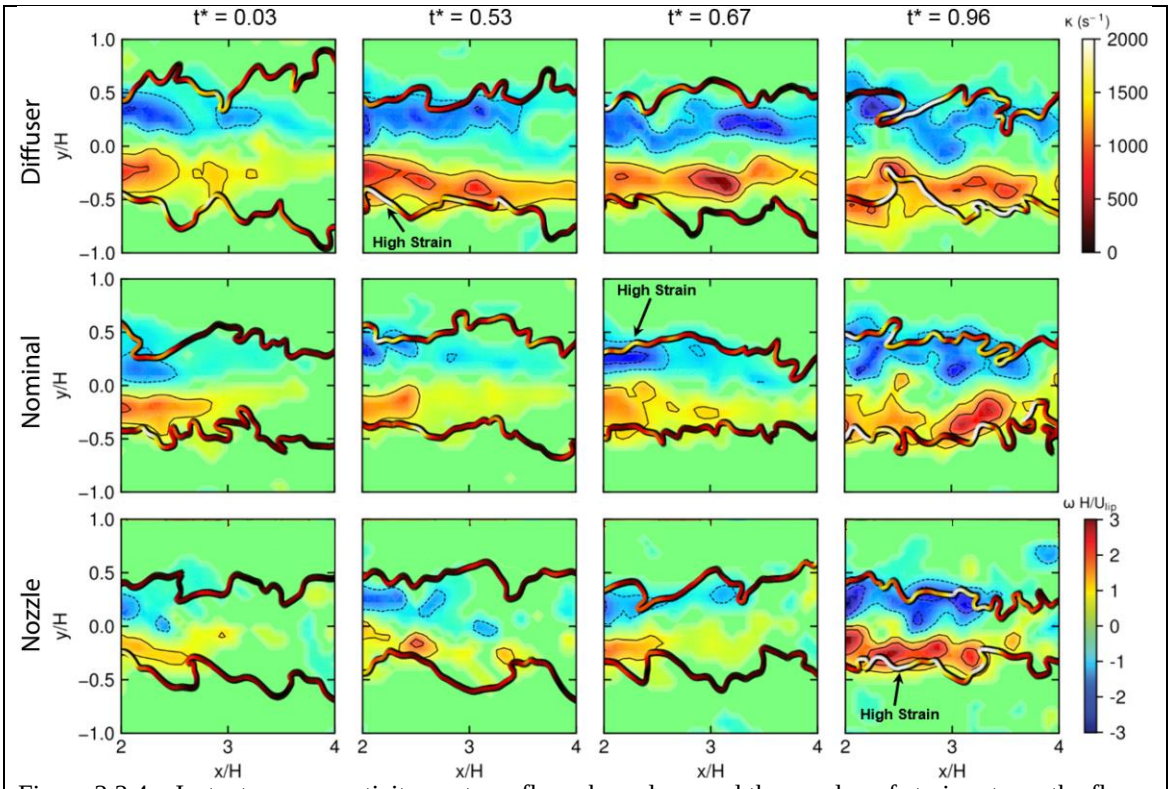

Figure 2.2.4 – Instantaneous vorticity contour, flame boundary, and the overlay of strain rate on the flame boundary. Time t* = 0 represents stable flame and t* = 1 is complete blow-out.

The measurements and related analysis generated in from this measurement campaign have been published in the journal Combustion and Flame and submitted to the (peer-reviewed) journal Proceedings of the Combustion Institute. They have also been presented at several scientific and technical meetings. The reader is referred to these publications for a more detailed description of the scientific findings;

Journal Publications

1. A.J. Morales, J. Reyes, K. Ahmed, I. Boxx. (2020). "Turbulent-Induced Blowout Mechanisms of Lean Bluff-Body Flames", Proc. Combust. Inst. – *Submitted, under review*
2. A.J. Morales, J. Reyes, P.H. Joo, I. Boxx, K. Ahmed. (2020). "Pressure Gradient Tailoring Effects on the Mechanisms of Bluff-Body Flame Extinction". Combust. Flame 215. (2020). 224-237

Conference Papers

1. I.M. Lasky, A.J. Morales, J. Reyes, K.A. Ahmed, I.G. Boxx. "The Characteristics of Flame Stability at High Turbulence Conditions in a Bluff-Body Stabilized Combustor", AIAA 2019-1734. AIAA SciTech 2019 Forum. 7 – 11 January, 2019. San Diego, California.
2. A.J. Morales, I.M. Lasky, J. Reyes, K.A. Ahmed, I.G. Boxx. "Controlling Flame Stability in a High-Speed Combustor through Pressure Gradients", AIAA 2019-1733. AIAA SciTech 2019 Forum. 7 – 11 January, 2019. San Diego, California.

Section 2.3 - Joint measurement campaign with Professor Venkat Narayanaswamy of North Carolina State University, on distributed flames and fluid structure interactions

Introduction / Background

In April, 2019, I travelled to Rayleigh, North Carolina to conduct a joint measurement campaign with Professor Venkat Narayanaswamy of the North Carolina State University. This campaign was three weeks in duration. The goal of this campaign was twofold. As with the first two external measurements campaigns, the primary goal was to transfer knowledge, experience and "know-how" about laser diagnostic imaging techniques with another AFOSR-supported research team. The secondary goal for this collaboration was help design, build up and conduct laser imaging measurements of flames in the distributed reactions regime and to study fluid-structure interactions in a supersonic wind tunnel. These goals were largely achieved during my stay at Professor Narayanaswamy's laboratory. The collaboration may therefore be considered a success.

Combustion Experiment

The first (of two) experimental setups I worked on with Professor Narayanaswamy's group at NC State University was a combined PIV / HCHO-PLIF / CH* chemiluminescence imaging system focused on a jet-in-vitiated co-flow (JIVCF) burner. The goal of this study was to understand the turbulence chemistry interactions associated with the regime transition of a conventional flame into distributed reaction combustion.

Burner

Figure 2.3.1 shows a schematic diagram of the JIVCF burner. The JIVCF burner was designed to approximate the Vitiated Coflow Burner (VCB) used by Cabra et al. [13]. In this burner, a jet of fuel (propane, ethylene or a mixture thereof) is delivered through a 5mm (inner diameter) tube into a co-flowing stream of hot combustion products generated by a lean, methane-air flame stabilized on a ceramic honeycomb plate upstream. As can be seen in Figure 2.3.1, the combustion products pass through another ceramic honeycomb flow condition prior to entering the measurement region. This has the effect of both straightening/homogenizing the velocity profile of the coflow and cooling it somewhat. The coflow temperature is controllable by varying the stoichiometry of the vitiator. The standard deviation of temperature across the coflow section is ≈ 22 K.

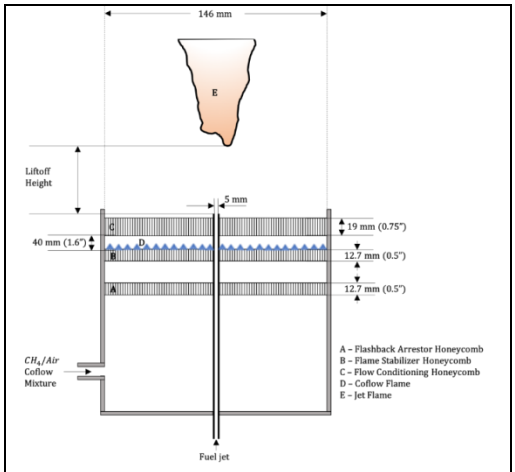

Figure 2.3.1 – Schematic of the Jet in Vitiated Coflow (JIVCF) Burner studied at NC-State University.

HCHO-PLIF / CH Imaging System*

The HCHO-PLIF system consisted of a frequency-tripled, flashlamp-pumped Nd:YAG laser with an energy of ≈ 170mJ/pulse and pulse duration of 10ns. A combination of cylindrical and spherical lenses was used to form a 25 mm tall sheet out of the laser beam. This sheet was used to excite the $\tilde{A}^1 A_2$ - $\tilde{X}^1 A_1$ 4_0^1 transition of formaldehyde, which is a commonly used excitation scheme [14-17]. A frame straddling ICCD camera (Princeton Instruments Inc., Model PI-MAX4), operating at 10 Hz and fitted with a Nikkor 50 mm f/1.2 lens, was used to acquire the fluorescence at an exposure time of 50 ns. A 425 nm bandpass interference filter with 50 nm full width at half maximum (FWHM) was used to detect fluorescence from the emission bands in this wavelength range.

For each measurement, the first frame imaged onto the ICCD camera contained the HCHO-PLIF signal. The second frame captured the CH*-chemiluminescence from the jet flame, with an exposure time of 250 μs. The chemiluminescence image was acquired 5 μs after the PLIF image. An in-house developed Matlab code was used to binarize both PLIF and chemiluminescence images and compute

the areas of the formaldehyde region and regions of CH*-chemiluminescence respectively based on the number of non-zero pixels in each image.

Stereo-PIV System

The SPIV system consisted of a dual-cavity, flashlamp-pumped Nd:YAG laser and a pair of compact CCD cameras (PCO Pixelfly USB). The laser beam was formed into a thin sheet using a spherical and a cylindrical lens, overlapped with the 355nm beam of the HCHO-PLIF imaging system and directed into the measurement region of the test stand.

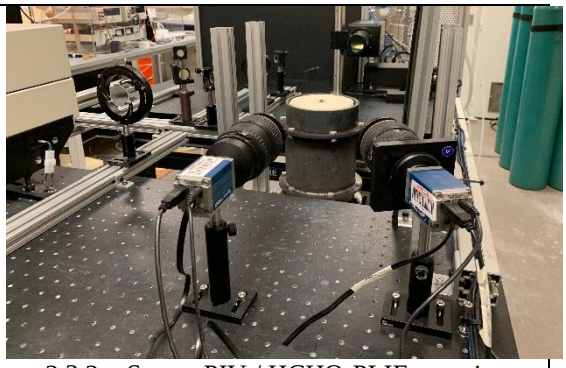

Figure 2.3.2 – Stereo-PIV / HCHO-PLIF experiment implemented at Professor Narayanaswamy's laboratory at NC State University.

The CCD cameras have a much lower acquisition rate than the highspeed CMOS systems used in other experiments in this project, but are nonetheless quite capable in their own right, with 1392 × 1040 pixel imaging arrays, 6.45 × 6.45 µm pixels and 14 bit dynamic range. The cameras were equipped with 100mm, f/2.8 macro lenses (Tokina). Both cameras were mounted on one side of the laser sheet, with one looking normal to the direction of propagation and the other at approximately 30 degrees off-normal, in a forward scattering configuration. The reason for this unconventional imaging configuration was that only one scheimpflug adaptor (necessary for the correction of blur associated with off-axis imaging) was available at the time for this experiment.

Test Cases

Although I had to return to Stuttgart shortly after the experimental system described above was set up and aligned, Professor Narayanaswamy's students were able to put it to good use shortly thereafter to acquire a high quality set of measurements on the jet flame in hot coflow.

The experimental parameters measured in this study are listed in Table 1. Three cases were tested with different fuels in the jet and under slightly different coflow conditions. The coflow comprised of products from a flat premixed methane/air flame. For the propane jet, the jet Reynolds number was increased steadily with time by increasing the fuel flow rate in an approximately linear manner. For the ethylene-propane case, the ethylene flow rate was maintained constant, corresponding to Re_D = 2000, while the propane flow rate was increased approximately linearly. The third case was of a fixed Reynolds number ethylene flame. PIV, PLIF, and CH* chemiluminescence images were obtained simultaneously as the jet flow rate (thus Re_D) was increased.

Table 1: Experimental Parameters

Jet Fuel	Coflow Equivalence Ratio (ϕ)	Coflow Velocity (V_{co})	Coflow Temperature (T_{co})	Coflow Oxygen Mole Fraction (X_{O_2})	Jet Reynolds Number (Re_D)
Propane	**0.65**	0.20 m/s	990 K	7 %	3,900 - 4,700
Ethylene -Propane	**0.60**	0.20 m/s	988 K	8 %	2,850 – 7,050 (and 10,000)
Ethylene	**0.60**	0.20 m/s	988 K	8%	5,900

Flow-Structure Interaction in a Supersonic Wind Tunnel

In addition to the combustion experiment described above, during my visit I helped design and implement a measurement system to study the fluid structure interactions of a panel with an incident shock wave. This measurement system is able to simultaneously acquire stereo-PIV and pressure sensitive paint measurements at the wall of a supersonic wind tunnel. Each system is described (separately) below.

Supersonic Wind Tunnel

This experiment was set up at the supersonic wind tunnel facility at North Carolina State University. This is a Mach 2.5, blowdown tunnel and has a constant-area test section measuring 150 mm × 150 mm × 650 mm. Each run lasted 6 s with a stagnation temperature of approximately 300 K and a constant stagnation pressure of 450 kPa. The stagnation temperature was assumed to be constant during the run given the wind tunnel's low enthalpy conditions. These conditions give a freestream unit Reynolds number of approximately 5.3 × 107/m.

For this experiment, one wall of the tunnel was replaced with a cavity covered by a thin, flexible panel. The purpose of this was to study shock/structure interaction along a surface subject to static deformation. This flow configuration has important implications for understanding shock/structure interaction in flight vehicles, which typically have thin (and thus deformable) skins.

PIV System

The PIV system consisted of a dual-cavity, flashlamp-pumped Nd:YAG laser (Continuum Surelite PIV) and a pair of CCD cameras (pco.2000). The laser has a repetition rate of 10 Hz, and delivers approximately 80 mJ/pulse at 532 nm. The beam was directed into the test section of the supersonic wind tunnel via a periscope, after having been formed into a thin sheet using spherical and a cylindrical lens.

Depending upon the specific requirements of the measurement, and the availability of the (shared) camera equipment, the PIV system could be quickly aligned in one of two configurations simply by moving one of the two CCD cameras higher or lower on its mounting post. In stereo-PIV configuration the cameras were both equipped with 180mm, f/3.5 macro lenses (Tamron) and were oriented above the laser sheet looking down toward the tunnel wall. In this configuration, both cameras are equipped with scheimpflug adaptors to correct blur associated with off-axis imaging. The objective lenses and scheimpflug adaptors were generously loaned to us for the campaign by AFRL employee (and long-term collaborator) Dr. Campbell Carter.

In the second imaging configuration, one CCD camera is used for PIV imaging, again with a 180mm, f/3.5 macro objective lens. The second camera is then lowered on the mounting post to image approximately perpendicular to tunnel wall (as shown in Figure 2.3.3). In this configuration, the second camera is used for imaging the pressure sensitive paint.

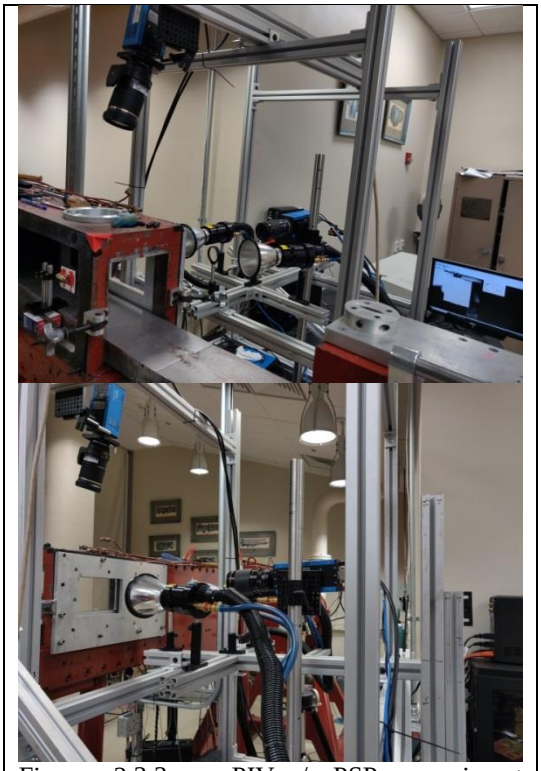

Figure 2.3.3 – PIV / PSP experiment implemented at Professor Narayanaswamy's laboratory at NC State University. In this configuration, the upper camera is used for near-wall PIV imaging and the lower camera images the pressure sensitive paint.

Pressure Sensitive Paint System

The pressure sensitive paint system consists of three main components, 1) the paint itself, 2) a high intensity UV-illumination system and 3) an imaging system. The pressure sensitive paint, applied to the flexible wall of the wind tunnel, was a commercially available variety, supplied by Innovative Scientific Solutions Inc. The paint was illuminated using a pair of water-cooled UV flashlamps (also supplied by ISSI, LM2X-400 LED modules) operated at 100% duty cycle. Multiple illumination sources were needed when recording at high frame-rates but also gives flexible and uniform illumination for low framerate acquisition. PSP signal was imaged using one of two camera systems available at Professor Narayanaswami's laboratory. For high spatial resolution imaging at 10 Hz acquisition rate, a CCD camera (pco.2000) was used. For low-to-moderate spatial resolution at high acquisition rate, a highspeed CMOS camera (Photron SA-X2) was used. For high resolution imaging, a 105mm, f/2.5 macro objective (Vivitar) was used. For highspeed imaging, a 50mm, f/1.2 objective (Nikon) is used.

Preliminary Results

My primary task during this collaboration was to help design, set up and align the measurement systems. As such, I was not present during the actual measurement presented below. That being said, however, by the time I returned from my trip to Professor Narayaswamy's laboratory the PIV / PSP imaging system was set up, aligned and ready for use. After my departure, Professor Narayanaswamy's students successfully deployed this measurement system to acquire measurements of a shock wave impinging on the flexible panel mounted in the wind tunnel. A sample of these measurements is presented below, in Figure 2.3.4.

Measurements and analysis of this exciting test case are still ongoing at the time of writing. It is planned to submit a paper based on the first results from this study before the end of the year.

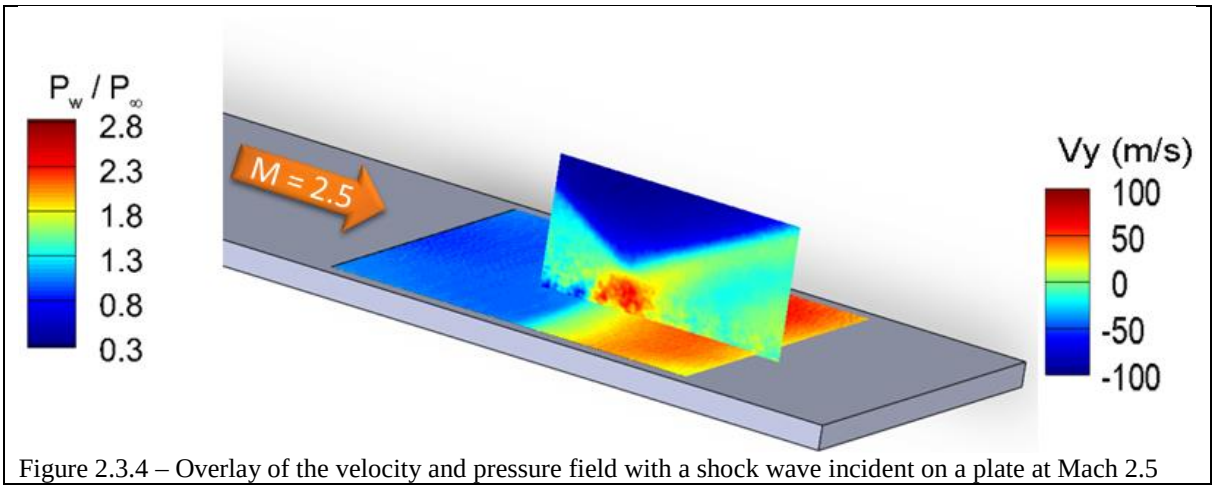

Figure 2.3.4 – Overlay of the velocity and pressure field with a shock wave incident on a plate at Mach 2.5

Conclusions

This project had the following three key goals;

1. To explore the viability of applying simultaneous, kHz-rate stereoscopic particle image velocimetry (stereo-PIV) and planar laser-induced fluorescence of hydroxyl (OH-PLIF) in a lean, turbulent swirl-stabilized flame at pressures ranging from 5 bars up to those found in a modern gas turbine combustor.
2. To apply these diagnostics to study flow-flame interactions leading to combustion instability and thermo-acoustic pulsation in the DLR Dual-Swirl Burner and a premixed, bluff-body stabilized flame at elevated pressure conditions.
3. To share the knowledge and experience gained in this project with members of the AFOSR-Basic Combustion Research Program and the wider combustion research community through a series of one-on-one, on-site technical collaborations.

All three objectives were successfully achieved. High bandwidth laser imaging demonstrated in turbulent swirl- and bluff-body stabilized flames at pressures of up to 20 bars. Detailed, multi-diagnostic measurements were acquired in swirl- and bluff-body stabilized flames at elevated pressures. These measurements generated significant new insight into the turbulent mixing and flame dynamics, combustion instabilities and flow-flame interaction. In addition, three external measurement campaigns were completed at universities in the United States. During these campaigns, the research teams of young faculty (sponsored through the AFOSR-BCR program) received both hands-on training and valuable practical experience in the design, setup and operation of sophisticated laser diagnostic systems for combustion research. The research produced in this project has resulted in five peer-reviewed journal papers, with two more currently under review and several more now in preparation. In addition, it has generated nine conference proceedings.

References

1. R. Balachrandran, B.O. Ayoola, C.F. Kaminski, A.P. Dowling, E. Mastorakos. Combust. Flame. 143, (2005) 37-55.
2. K.P. Geigle, R. Hadef, W. Meier. J. Eng. Gas Turbines Power 136 (2014) 021505.
3. K.P. Geigle, M. Köhler, W. O'Loughlin, W. Meier. Proc. Comb. Inst. 35 (2015) 3373.
4. I.G. Boxx, C.D. Carter, K.-P.Geigle, W. Meier., 54th AIAA Aerospace Sciences Meeting, AIAA SciTech Forum, AIAA 2016-0435.
5. M. Stöhr, C. Arndt, W. Meier. Proc. Combust. Inst. 34 (2013) 3107–3115.
6. Y. Hardalupas, and M. Orain, Combust. Flame 139 (2004) 188-207.
7. S. Mallat, 1998, A Wavelet Tour of Signal Processing, Academic Press
8. J. Lewalle, Farge, M. and K. Schneider, 2007, Wavelets, in Springer Handbook of Experimental Fluid Mechanics, Springer Verlag, 2007.
9. I. Boxx, C.D. Carter, K.-P. Geigle, W. Meier, B. Akih-Kumgeh, J. Lewalle. Proc. ASME 2017 Turbo Expo, June 26 – 30, 2017. GT2017-64438. (2017).
10. I. Boxx, C.D. Carter, K.-P. Geigle, B. Akih-Kumgeh, J. Lewalle. AIAA SciTech 2017. January 9 – 13th, 2017.
11. P.E. Roach, Int. J. Heat and Fluid Flow 8 (2) (1987) 82-92.
12. Reyes, J., Kailasanathan, R. K. A., and Ahmed, K., Energy & Fuels 32 (2018) 10933-10940.
13. R. Cabra, J.Y. Chen, R.W. Dibble, A.N. Karpetis, R. Barlow. Combust. Flame 143:4, (2005) 491–506.
14. B. Zhou, M. Costa, Z. Li, M. Aldén, and X. S. Bai. Proc. Combust. Inst. 36 (2017) 4305–4312.
15. C. Brackmann, J. Nygren, X. Bai, Z. Li, H. Bladh, B. Axelsson, I. Denbratt, L. Koopmans, P. Bengtsson, M. Alden. Spectrochim. Acta - Part A Mol. Biomol. Spectrosc. 59 (2003) 3347–3356.
16. R. L. Gordon, A. R. Masri, Mastorakos. Combust. Flame. 155 (2008), 181–195.
17. S. A. Skeen, J. Manin, L. M. Pickett. Proc. Combust. Inst. 35 (2015) 3167–3174, 2015.

Publications

Scientific / Technical Journals (Peer-reviewed)

1. I. Litvinov, J. Yoon, C. Noren, M. Stöhr, I. Boxx, K.P. Geigle. (2020) "Time-resolved study of mixing and reaction in an aero-engine model combustor at increased pressure". Combust. Flame. – *Under review*
2. A.J. Morales, J. Reyes, K. Ahmed, I. Boxx. (2020). "Turbulent-Induced Blowout Mechanisms of Lean Bluff-Body Flames", Proc. Combust. Inst. – *Under review*
3. A.J. Morales, J. Reyes, P.H. Joo, I. Boxx, K. Ahmed. (2020). "Pressure Gradient Tailoring Effects on the Mechanisms of Bluff-Body Flame Extinction". Combust. Flame 215. (2020). 224-237.
4. Tyagi, A., Boxx, I., Peluso, S., O'Connor, J. (2020) "Pocket formation and behavior in turbulent premixed flames". Combust. Flame 211, pp. 312-324.
5. A. Tyagi, I. Boxx, S. Peluso, J.O'Connor. (2019). "Statistics and Topology of Local Flame-Flame Interactions in Turbulent Flames", Combust. Flame 203 (2019), 92-104
6. M. Stöhr, K.P. Geigle, R. Hadef, I. Boxx, C.D. Carter, M. Grader, P. Gerlinger (2018). "Mechanisms of transient formation and oxidation of soot in an aero-engine model combustor", Proc. Combust. Inst. 37:4 (2018), 5421-5428.
7. A. Tyagi, I. Boxx, S. Peluso, J.O'Connor (2018). "The role of flow interaction in flame-flame interaction events in a dual burner experiment", Proc. Combust. Inst. 37:2 (2018). 2485-2491.

Techical Conferences, Symposia, Workshops (With Paper)

1. A. Ghani, W. Polifke, C. Noren, I. Boxx. „"Data-driven identification of nonlinear flame models". Proceedings of the ASME 2020 Turbo Expo GT2020, June 22-26, 2020, London, UK. – *Accepted, not yet in print.*
2. A. Tyagi, I.G. Boxx, S. Peluso, J. O'Connor. "Statistics of Local Flame-Flame Interactions in Flame Interaction Zones of Two V-Flames", AIAA-2019-0446. AIAA SciTech 2019 Forum. San Diego, California.
3. I.M. Lasky, A.J. Morales, J. Reyes, K.A. Ahmed, I.G. Boxx. "The Characteristics of Flame Stability at High Turbulence Conditions in a Bluff-Body Stabilized Combustor", AIAA 2019-1734. AIAA SciTech 2019 Forum. 7 – 11 January, 2019. San Diego, California.
4. A.J. Morales, I.M. Lasky, J. Reyes, K.A. Ahmed, I.G. Boxx. "Controlling Flame Stability in a High-Speed Combustor through Pressure Gradients", AIAA 2019-1733. AIAA SciTech 2019 Forum. 7 – 11 January, 2019. San Diego, California.
5. A. Tyagi, I.G. Boxx, S. Peluso, R. Shupp, J. O'Connor. "Structure of flames in flame interaction zones", AIAA 2018-0161. 2018 AIAA Aerospace Sciences Meeting, 8 – 12 January, 2018. Kissimmee, Florida.
6. J. Lewalle, I.G. Boxx, K.P, Geigle, C.D. Carter. "About an axisymmetric mode and a helical mode in the stable state of a model combustor", AIAA 2018-1877. 2018 AIAA Aerospace Sciences Meeting, 8 – 12 January, 2018. Kissimmee, Florida.
7. I.G. Boxx, K.P, Geigle, C.D. Carter, W. Meier, B.A. Kumgeh, J. Lewalle. "A study of spontaneous transition in swirl-stabilized flames". GT2017-64438. Proceedings of the ASME 2017 Turbo Expo IGTI 17 June 26-30, 2017, Charlotte, North Carolina, USA
8. I.G. Boxx, K.P, Geigle, C.D. Carter, M.H. Yang, J. Lewalle, B.A. Kumgeh, "Self-induced transitions between stable and thermoacoustically excited states in a model swirl-stabilized burner at elevated pressure", AIAA 2017-1102. 55th AIAA Aerospace Sciences Meeting, 9 – 13 January, 2017. Grapevine, Texas.
9. I.G. Boxx, C.D. Carter, K.-P. Geigle, W.Meier. "Effects of Air Staging on the Dynamics of an Ethylene-fueled Gas Turbine Model Combustor at Elevated Pressure", 18th International

Symposium on Applications of Laser and Imaging Techniques to Fluid Mechanics. 4 – 7 July, 2016. Lisbon, Portugal.

Techical Conferences, Symposia, Workshops (With Poster)

1. C. Noren, P. Saini, I. Boxx. "High bandwidth laser imaging measurements of premixed, turbulent bluff-body stabilized flames". 29. Deutscher Flamentag. 17-18 September, 2019. Bochum, Germany.